

Utah State University

DigitalCommons@USU

All Graduate Theses and Dissertations


Graduate Studies

5-1998

All-Sky Measurements of the Mesospheric "Frontal Events" From Bear Lake Observatory, Utah

Seon-Hee Seo
Utah State University

Follow this and additional works at: <https://digitalcommons.usu.edu/etd>

 Part of the [Physics Commons](#)

Recommended Citation

Seo, Seon-Hee, "All-Sky Measurements of the Mesospheric "Frontal Events" From Bear Lake Observatory, Utah" (1998). *All Graduate Theses and Dissertations*. 3838.

<https://digitalcommons.usu.edu/etd/3838>

This Thesis is brought to you for free and open access by the Graduate Studies at DigitalCommons@USU. It has been accepted for inclusion in All Graduate Theses and Dissertations by an authorized administrator of DigitalCommons@USU. For more information, please contact digitalcommons@usu.edu.



ALL-SKY MEASUREMENTS OF THE MESOPHERIC "FRONTAL EVENTS"
FROM BEAR LAKE OBSERVATORY, UTAH

by

Seon-Hee Seo

A dissertation submitted in partial fulfillment
of the requirements for the degree

of

MASTER OF SCIENCE

in

Physics

Approved:

UTAH STATE UNIVERSITY
Logan, Utah

1998

ABSTRACT

All-Sky Measurements of the Mesospheric "Frontal Events"

from Bear Lake Observatory, Utah

by

Seon-Hee Seo, Master of Science

Utah State University, 1998

Major Professor: Dr. Michael J. Taylor
Department: Physics

Studies of internal gravity waves in the earth's upper atmosphere are of considerable interest. These waves play a very important role in the dynamics of the mesosphere and lower thermosphere (MLT) region where they can transfer large amounts of energy and momentum from the lower atmosphere via wave saturation and dissipation. In particular, small-scale short-period (<1 hour) waves of the type regularly recorded by all-sky nightglow imagers operated by Utah State University (USU) are known to be very important contributors. In this thesis attention is focused on a subset of small-scale wave phenomena recently discovered using such image data, the so called "frontal events." Frontal events have distinguishable characteristics from usual short-period (<1 hour) gravity waves. The principal characteristics are a well defined leading "front," which exhibits a sharp change in intensity followed by a coherent wave trail (often extending from horizon to horizon) and relatively high phase speeds (>50

ms^{-1}). Another unusual characteristic of "frontal events" is an apparent reversal in contrast of the wave structures as imaged in the hydroxyl (OH) emission (peak altitude ~ 87 km) when compared with the oxygen (OI) "green line" (557.7 nm) emission (peak altitude ~ 96 km) that can sometimes occur. In one isolated case, observed from Haleakala, Hawaii, the bright wave crests in the OH emission appeared to propagate through a dark structureless sky, whereas in the OI emission the same waves appeared to propagate into a bright sky, leaving an apparently depleted emission in its wake. Recent theoretical studies based on noble measurements have shown that frontal events may be due to a "bore-like" intrusion that raises the OI (557.7 nm) layer by a few km and at the same time depresses the OH layer by a similar amount. However, studies of fronts and bores in the MLT region are exceptionally rare.

I have discovered and analyzed 16 frontal events from image data recorded at Bear Lake Observatory, Utah (41.6°N, 111.6°W), over the past four years. I have investigated some of their properties such as their horizontal wavelengths, horizontal phase speeds, observed periods, and their directions of motion. In addition, I have made comparative measurements of their relative intensities in the OH and OI emissions. These studies provide the first "extensive" data set on such events detailing their morphology and dynamics and should provide important information necessary for a deeper understanding of their occurrence frequency and properties.

ACKNOWLEDGMENTS

I am glad to thank my advisor, Dr. Michael J. Taylor, for all his efforts, guidance, patience, and encouragement for me to finish my thesis. I would like to emphasize that this thesis would not have been published without his helpful information and advice on my research. He introduced me to atmospheric physics, which I had never considered as my research topic before. I think this was a valuable and enjoyable experience for my future advanced study.

Technically, I am indebted to his wife, Visnja Taylor, for helping me whenever I was in trouble with the computer. The data analysis was performed using software developed by her. My thanks also goes to my two other committee members, Dr. William Pendleton, Jr. and Dr. Farrell W. Edwards, for overseeing my thesis development and giving me their precious feedback. In addition, I appreciate Dr. Bela G. Fejer's valuable and sincere advice and general guidance during my studies at Utah State University (USU). I also want to extend my thanks to Donna Eckburg, once an advisor at the USU Physics Department and now in Georgia, and Robert Davies, a graduate student in the USU Physics Department. They enriched my life in USU with their general help and kindness.

My special thanks goes to my spiritual leader, SungHo Lee, who has always prayed for me since I have known him, and my friends, June Lee, Ashley Kim, and ManBin Song, who have helped me in variety of ways during my studies at Logan.

Most of all, I would like to give my whole-hearted thanks to my parents in Korea, who have always been concerned about my health and education. With their special care and love for me, I was able to finish my thesis without any major troubles.

Finally, I acknowledge Dr. Taylor's grant from the National Science Foundation CEDAR Program Grant No. ATM-9525815, which enabled me to perform this research.

Seon-Hee Seo

CONTENTS

	Page
ABSTRACT	ii
ACKNOWLEDGMENTS	iv
LIST OF TABLES	viii
LIST OF FIGURES	ix
CHAPTER	
1. INTRODUCTION	1
1.1. Introduction To the Upper Atmosphere	1
1.2. Airglow Emissions	4
1.2.1. OH Emission	8
1.2.2. Green Line OI (557.7 nm) Emission	8
1.2.3. Na D Line Emissions	10
1.3. Gravity Waves	12
1.3.1. Introduction	12
1.3.2. Theory of Gravity Waves	15
1.3.3. Properties of Gravity Waves	20
1.4. Thesis Topic	22
2. IMAGING GRAVITY WAVES	23
2.1. Review of Gravity Wave Imaging	23
2.2. The Utah State University All-Sky Nightglow Imager	28
2.3. Types of Short Period Gravity Waves	30
2.3.1. Bands	31
2.3.2. Ripples	31
3. "FRONTAL EVENTS"	33
3.1. Introduction	33

3.2. Summary of ALOHA-93 Front-Like Data.....	34
3.2.1. Description of Image Data.....	34
3.2.2. Measurements of Wave Parameters.....	36
3.2.3. Relative Intensity Measurements.....	38
3.2.4. Summary of ALOHA-93 Event Characteristics.....	40
4. MID-LATITUDE MEASUREMENTS OF "FRONTAL EVENTS".....	41
4.1. Bear Lake Observatory.....	41
4.2. Image Analysis.....	43
4.3. Criteria for Identifying Frontal Events.....	44
4.4. Examples of Bear Lake Frontal Events.....	44
4.4.1. 21 January 1994.....	44
4.4.2. 4 May 1994 (two frontal events).....	45
4.4.3. 10 February 1995.....	49
4.4.4. 23 January 1996.....	50
4.4.5. 23 June 1996.....	50
4.4.6. 6 July 1997.....	53
4.5. Bear Lake Frontal Event Occurrence Frequency.....	54
5. RESULTS.....	57
5.1. Determination of Wave Characteristics.....	57
5.2. Intensity Measurements of Frontal Events.....	59
6. DISCUSSION.....	68
6.1. Mesospheric Bores.....	68
6.2. Comparison with Bore Theory.....	72
7. CONCLUSIONS AND RECOMMENDATIONS FOR FUTURE STUDIES.....	75
REFERENCES.....	78
APPENDIX.....	85

LIST OF TABLES

Table	Page
2.1 Characteristics of the Filters Used for the All-Sky Nightglow Measurements	30
3.1 Horizontal Wave Parameters for Each of the Four Nightglow Emissions Recorded on 10 Oct. 1993 During the ALOHA-93 Campaign.....	38
4.1 Bear Lake Frontal Event Monthly Occurrence	55
5.1 Summary of Derived Wave Parameters for 16 Frontal Events Imaged at Bear Lake Observatory, Utah.....	57
5.2 Contrast Measurements of the Front and Trailing Waves of 16 Frontal Events.....	60

LIST OF FIGURES

Figure	Page
1.1 Temperature distribution and nomenclature of the earth's atmosphere.....	2
1.2 Plots of some fundamental properties of the atmosphere as a function of height.....	3
1.3 Nightglow spectrum from 500 to 800 nm.....	6
1.4 Volume emission rate as a function of altitude.....	7
1.5 Sketch of the energy-level diagram of atomic oxygen.....	9
1.6 Sketch of the energy-level diagram for the Na atom.....	11
1.7 Relationship between wavelength, velocity, and propagation angle.....	17
1.8 Dispersion curves for an AGW showing the acoustic and the gravity wave regions.....	19
1.9 Contours of constant period in the k_x - k_z domain.....	19
1.10 Pictorial representation of an internal atmospheric gravity wave.....	20
1.11 Propagation characteristics of gravity waves into the upper atmosphere.....	21
2.1 Long exposure near infrared photograph showing "cloud-like" OH structures at $\sim 15^\circ$ elevations over New Mexico.....	24
2.2 Two narrow field CCD images, showing (a) "bands" and (b) "ripples" imaged in the near infrared OH emission from Haleakala Crater, Maui, HI, during the ALOHA-90 campaign.....	26
2.3 All sky "difference image" showing a coherent wave pattern recorded in the NIR OH emission during the ALOHA-93 campaign.....	28
2.4 Schematic diagram showing the USU all-sky CCD imager.....	29
3.1 Sequence of all-sky CCD images showing OI (557.7 nm) (left) and NIR OH (right) (integration time for OI = 90 s, OH = 20 s).....	35
3.2 Ground map showing the geographic location and orientation of the OI wave pattern at 11:06 UT shortly after the front passed overhead.....	37

3.3	Map showing the orientation and motion of the OI wave front as it passed first over Kauai, Maui, and then Big Island during 130 min period	37
3.4	Relative intensity plot normal to the wave crests for the OH and OI data at zenith	39
4.1	Bear Lake Observatory, Utah (courtesy V. Wickwar)	42
4.2	Frontal event imaged in the OH, OI, Na emission layers (21 Jan. 1994)	46
4.3	A frontal event imaged in the OH emission layer (4 May 1994)	47
4.4	The same frontal event as shown in Figure 4.3 but now in the OI (557.7 nm) emission (4 May 1994)	48
4.5	A sharp edge with no trailing waves imaged in the OI (557.7 nm) emission (10 Feb. 1995)	50
4.6	A high-contrast frontal event imaged in the OH and OI (557.7 nm) emissions (23 Jan. 1996)	51
4.7	Unusual frontal event observed in the OH and OI (557.7 nm) nightglow emissions (23 June 1996)	52
4.8	Dual frontal events imaged in the OH and OI (557.7 nm) nightglow emissions (6 July 1997)	54
5.1	Intensity profiles of OH (top) and OI (bottom) emission at 13:05 UT 21 Jan. 1994, BLO (event 1)	62
5.2	Intensity profiles of OH (top) and OI (bottom) emission at 05:50 UT 4 May 1994, BLO (event 3)	63
5.3	Intensity profiles of OI emission at 11:02 UT 10 Feb. 1995, BLO	64
5.4	Intensity profiles of OH (top) and OI (bottom) emission at 02:57 UT 23 Jan. 1996, BLO (event 12)	65
5.5	Intensity profiles of OH (top) and OI (bottom) emission at 10:22 UT 23 June 1996, BLO (event 13)	66
5.6	Intensity profiles of OH (top) and OI (bottom) emission at 10:03 UT 6 July 1997, BL(event 15)	67
6.1	Undular tidal bore on the River Mersey, England	69

6.2	Schematic diagram showing a bore of height h_1-h_0 propagating to undisturbed water of depth h_0	70
6.3	Schematic diagram showing a symmetrical undular bore.....	71

CHAPTER 1

INTRODUCTION

1.1 Introduction to the Upper Atmosphere

The atmosphere can be classified into several regions termed troposphere, stratosphere, mesosphere, and thermosphere according to its temperature structure. Figure 1.1 shows the temperature-height distribution and nomenclature of the earth's atmosphere.

Most weather phenomena occur in the troposphere, and thus we are most familiar with it. In the troposphere the temperature decreases with altitude until it reaches an upper limit called the tropopause, which ranges in height from about 8 km to 15 km above the surface, depending on latitude. As the temperature decreases with altitude, the troposphere becomes unstable and strong convection--the source of our weather--results. In the stratosphere, which lies within about 50 km of the earth's surface, the temperature increases due to absorption of solar ultraviolet radiation by ozone. Thus the stratosphere is stable against convection. Above the stratosphere lies the mesosphere where the temperature again falls with height within the altitude range ~50 to 80 km. At higher altitudes the temperature rises again due especially, to absorption of solar far-ultraviolet radiation by atomic and molecular oxygen. The region of transition, termed the mesopause, is the coldest place on earth (reaching lower than 150 K in summer at high latitudes) and is dynamically driven by gravity waves, which are the subject of this thesis.

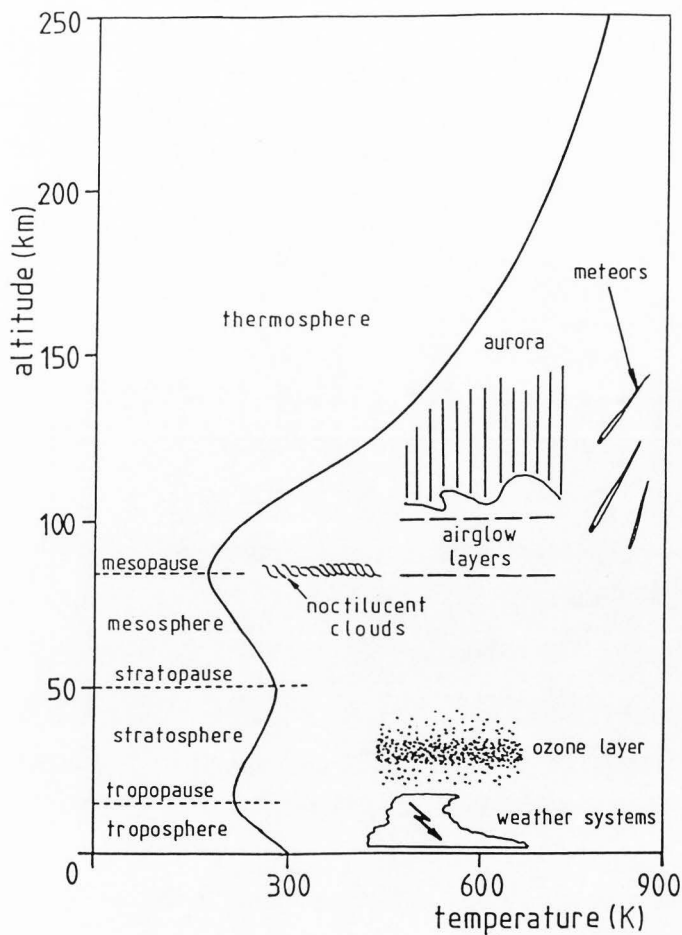


Figure 1.1 Temperature distribution and nomenclature of the earth's atmosphere [Taylor, 1986a].

Figure 1.2 plots some of the fundamental properties of the atmosphere as a function of height. At mesospheric and lower thermospheric (MLT) heights (~ 80 - 100 km), where the airglow layers exist (see Figure 1.1), the gas is very tenuous because the volume occupied is very large compared to the total mass of the upper atmosphere. The pressure of the upper atmosphere is also very low, essentially at a laboratory vacuum.

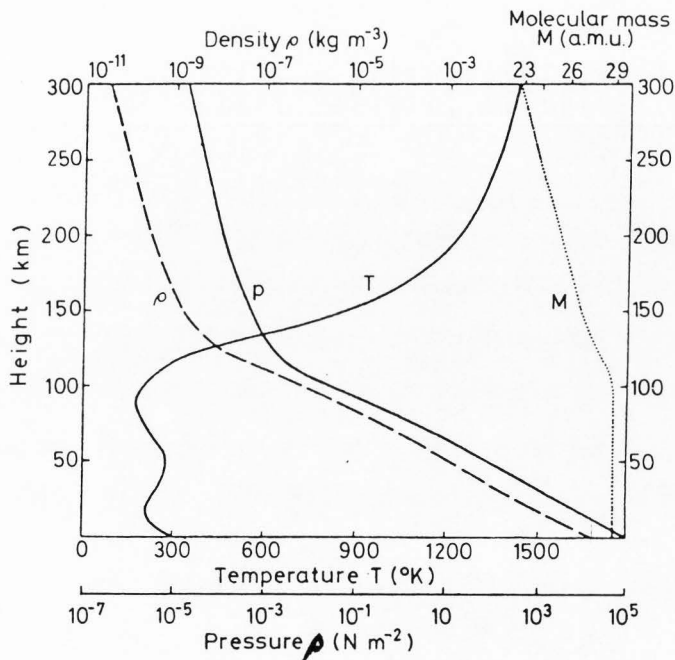


Figure 1.2 Plots of some fundamental properties of the atmosphere as a function of height [Hargreaves, 1979].

Ultraviolet radiation from the sun ionizes the upper atmosphere above ~80 km, creating the ionosphere. In this region photochemical processes involving electronic and ion production and loss in the presence of sunlight and other ionizing radiation dominate with increasing altitude. The increase in temperature of the thermosphere results from these photochemical processes, which release energy. The degree of solar activity, altitude, latitude, time of day, and season are all major variables in the upper atmosphere's thermal response. From the previous descriptions it is apparent that the upper atmosphere is very different from the troposphere in which we live.

1.2 Airglow Emissions

Otto Struve first suggested the term "airglow" to distinguish the light from aurora [Elvey, 1950]. The main energy source of airglow is the sun. Airglow is a phenomenon describing nonthermal radiation emitted by the atoms and molecules of the earth's upper atmosphere reacting together to give off light. On the other hand, auroral light results from impact on neutral atmospheric gases by charged particles penetrating down the earth's magnetic field. Airglow is classified into three categories: dayglow, twilight glow, and nightglow according to the time when they occur. Dayglow is generally difficult to observe because of direct sunlight even though the emissions of dayglow are the most intense among the three. Twilight glow occurs during the transition time between day and night and usually has a relatively short observing time, depending on the latitude of observation. There are several prominent nightglow emissions which are all due to the photochemical processes. In the MLT region the nightglow consists of several different line and band emissions occurring at visible, near

infrared (NIR) wavelengths. These emissions are significantly fainter than the dayglow and twilight glow but are relatively easy to investigate, due, in part, to the long observation times available.

The forbidden oxygen (OI) "green line" and the sodium "D line" doublet occur in the visible part of the spectrum and were studied first about 100 years ago. Figure 1.3 shows the nightglow spectrum from 500 to 800 nm. Note the relatively low intensity of the visible wavelength atomic line emissions and the abundance of molecular band emissions at NIR wavelengths due, primarily to the hydroxyl (OH) emission. The first detailed studies of the night sky spectra were made in the 1940's. In contrast, studies of the infrared and ultraviolet sky spectrum have primarily been made over the past 25 years with the development of more sensitive detectors. These measurements have revealed that the OH emission is the most intense airglow in the night sky; however, it occurs primarily at NIR and infrared wavelengths. Ground-based observation of the infrared airglow is limited by water vapor absorption in the atmosphere. However, observations at NIR wavelengths ($<1 \mu\text{m}$) are not significantly affected by water vapor and provide the bulk of the OH image measurements to date. The distribution of atmospheric constituents determines the specific airglow emission heights, such as the OH emission, which peaks at ~ 87 km and has a nominal nighttime half-width of ~ 6 to 8 km [Baker and Stair, 1988]. Similarly the Na emission originates at ~ 90 km and the OI emission at ~ 96 km, each with nominal half-width of <10 km. Figure 1.4 shows the normalized volume emission rates versus altitude for several MLT nightglow emissions.

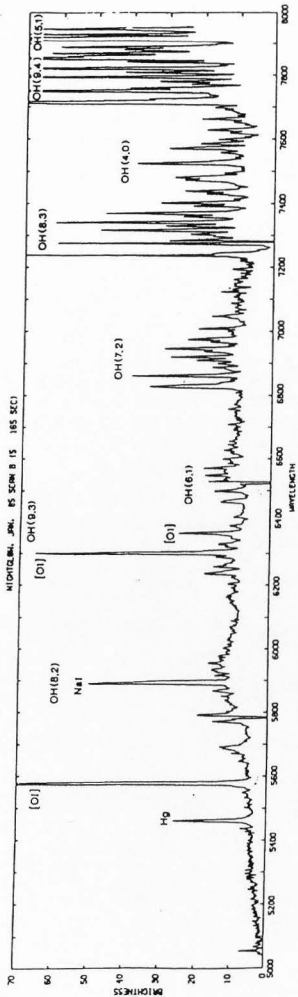


Figure 1.3 Nighglow spectrum from 500 to 800 nm [Rees, 1989].

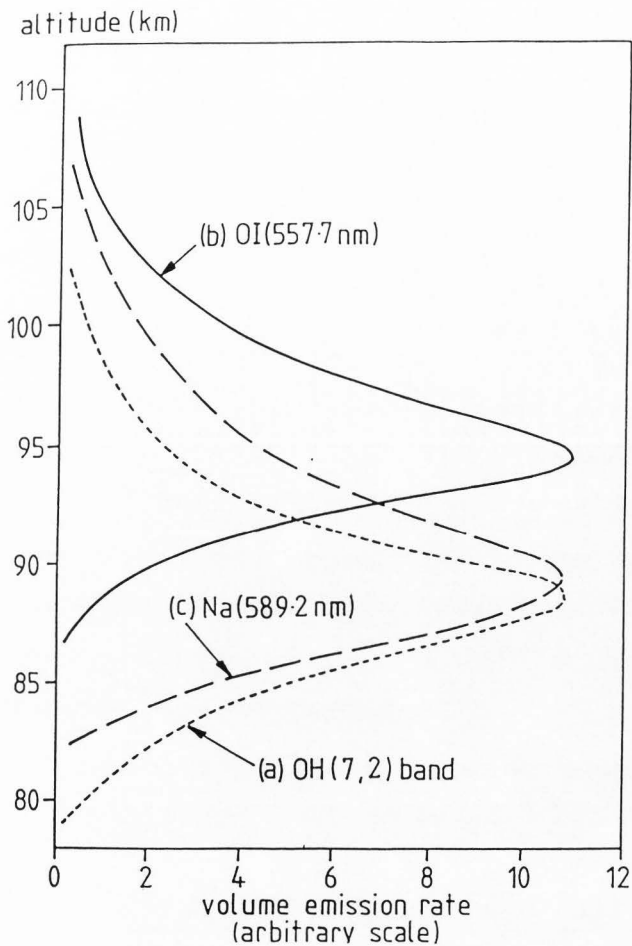


Figure 1.4 Volume emission rate as a function of altitude from *Taylor* [1986a].

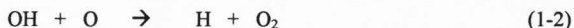
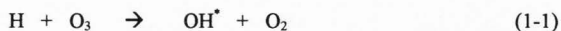
(a) the OH (7,2) band at 686 nm [*Watanabe et al.*, 1981]

(b) the OI line at 557.7 nm [*Greer and Best*, 1967]

(c) the Na line at 589.6 nm [*Greer and Best*, 1967]

1.2.1 OH Emission

Krassovsky obtained some of the first high resolution spectra of the night sky in 1949 revealing its complex emission structure. Later, *Meinel* [1950 a, b] determined the spectra was due mainly to rotational-vibrational transitions of the OH molecule in its ground state. *Bates and Nicolet* [1950] first suggested the "ozone mechanism" to explain the production of vibrationally excited OH:

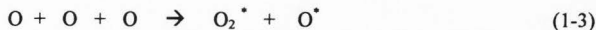


The asterisk represents OH in its vibrationally excited state ($v' < 9$). Examination of the equations (1-1) and (1-2) shows that this mechanism contributes to the destruction of ozone and atomic oxygen in the upper atmosphere while the hydrogen acts as a catalyst in these reactions. This excited OH gives rise to a series of rotational-vibrational bands extending from 0.4-4 μm which dominate the NIR spectrum. The intensity of the nighttime OH emission can vary considerably during the night and from night to night. The seasonal variations in the average mid-latitude intensity indicate a peak around November, and a minimum in the summer, around August [*Barbier and Glaume*, 1960].

1.2.2 Green Line OI (557.7 nm) Emission

Like the OH emission, the green line (557.7 nm) emission is present in the night sky at all latitudes and has in the past been called "permanent aurora" or "non-polar

aurora." *McLennan and Shrum* [1925] first identified the green line emission as due to the forbidden electronic transition $^1S_0 \rightarrow ^1D_2$ of oxygen atom. Figure 1.5 shows an energy-level diagram of the lowest electronic states of atomic oxygen. Unlike the OH Meinel band emissions, the green line emission originates from a single electronic transitions and results in a line spectra. Two competing mechanisms have been proposed to explain this nightglow. *Chapman* [1931] first proposed the "three body" atomic oxygen mechanism to explain the origin of this nightglow emission:



Barth and Hildebrandt's [1961] indirect mechanism was suggested as an alternative approach to explain the lack of observed green line emission in laboratory systems

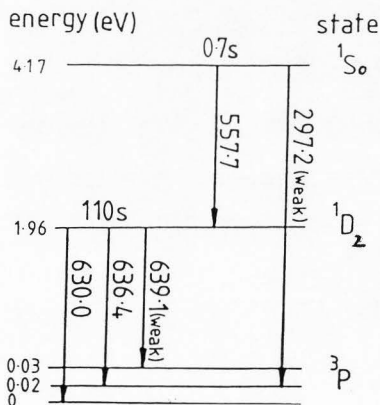
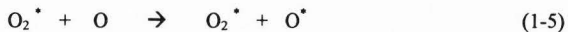
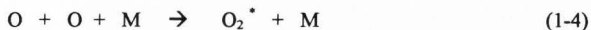


Figure 1.5 Sketch of the energy-level diagram of atomic oxygen.

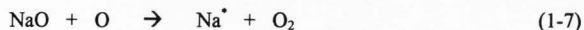
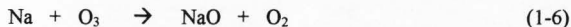
with oxygen atoms present:



In this reaction, M is an unspecified species (most likely N_2) helping two O atoms to make excited O_2 , which then plays an important role in forming an excited O atom in the ^1S state. The identity of the intermediate excited O_2 state is currently unknown. This mechanism is generally considered to provide the best explanation for the observed data. The seasonal variation in the intensity of this emission shows two peaks a year about a month after each solstice. On the other hand, the diurnal and day-to-day variations are similar to those of the OH emission [Roach and Smith, 1967].

1.2.3 Na D Line Emissions

Like the previous two emissions (OI and OH), the Na nightglow emission is due to photochemical processes in the night sky. During twilight and during the day, this emission results from resonant scattering of sunlight [Chapman, 1939]. The nightglow emission reactions are:



This two-stage process involves formation of NaO, which then reacts with atomic oxygen to form Na in its excited 2P state in either the $^2P_{1/2}$ or $^2P_{3/2}$ states, which then radiate to a ground 2S state, creating the characteristic Na doublet emission. Like the OI emission, the two Na emissions are electronic transitions and thus spectroscopy shows two closely spaced line spectra (see Figure 1.6). Na is the weakest of the three nightglow emissions discussed here, its integrated intensity is higher in the winter months, and it has been suggested that evaporating meteors or the upward convection of salt from the oceans are the primary sources for the Na atoms in the upper atmosphere.

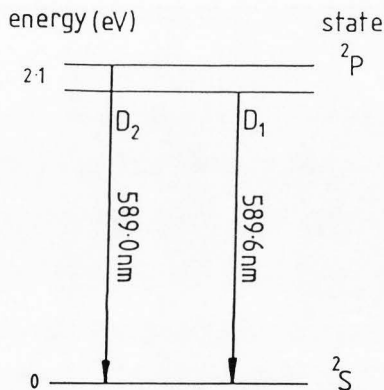


Figure 1.6 Sketch of the energy-level diagram for the Na atom.

1.3 Gravity Waves

1.3.1 Introduction

Atmospheric tides, planetary waves, and gravity waves are the three main perturbing phenomena of the MLT region. A tide is generated due to an external agent like the sun, and thus it keeps a constant relationship while the earth rotates beneath [Hargreaves, 1979]. Such tides are called migrating tides as they appear to move westward with the apparent motion of the sun. Atmospheric tides have dominant periods of 24, 12, and 8 hours but other harmonics have also been observed.

Planetary waves are even larger scale waves which are observed in the gaseous flow on a planetary scale and are generated due to variations in the Coriolis parameter with latitude [Houghton, 1989]. Prominent planetary waves with periods of about 2 days and 16 days have been identified in extensive radar data sets but other periodicities also exist. Gravity waves exhibit significantly shorter periods than tides and planetary waves but play a very important role in the dynamics of the middle atmosphere because they are most effective at transporting energy and momentum from the lower atmosphere (troposphere) to the mesopause region, where they release their energy and momentum as they saturate and eventually dissipate [e.g., Lindzen, 1981; Matsuno, 1982; Fritts and Rastogi, 1985; Nakamura *et al.*, 1996].

Gravity waves (or buoyancy waves as they are sometimes called) are "generated" by the force of gravity which acts on a displaced parcel of air. That is to say gravity is the primary restoring force of the waves. On the other hand, acoustic waves are generated by a change of pressure which acts on the medium compressed. However,

every atmospheric wave can be classified as an acoustic-gravity wave (AGW) since, in general, we must consider both the compressional and the gravitational restoring forces. At the high-frequency limit pure acoustic waves propagate only longitudinally, whereas pure gravity waves are the low-frequency limit of the AGW spectrum and exhibit transverse motion. Thus AGWs exhibit both longitudinal and transverse propagation characteristics. The most well-known example of gravity waves are surface waves that are trapped at the ocean surface and cannot propagate vertically. However, atmospheric gravity waves are "internal," which means they can propagate freely throughout the atmosphere. A good example of atmospheric gravity waves is seen in lenticular clouds which can form during periods of strong winds in the lee of mountains [Houghton, 1989]. In the case of the atmosphere, gravity waves arise due to variations in air density as a function of height. Internal gravity waves therefore tend to increase their amplitudes of oscillation as height increases (in proportion to the inverse of the square root of the density) as the energy flux will remain constant assuming no dissipation [Hines, 1960]. Thus, above ~75 km gravity waves are very prominent atmospheric motions, whereas they are considered minor perturbations in the lower atmosphere [Houghton, 1989]. In this thesis I focus attention on short period (<1 hour) gravity waves that are responsible for a large amount of the energy and momentum transported into the upper atmosphere [Fritts and Vincent, 1987].

The sources for short period gravity waves are postulated as tropospheric disturbances like jet streams, storms, weather fronts, the interaction of strong winds with large mountains and upper atmospheric sources like the auroral electrojet, strong particle

precipitation, and the in situ breakdown of large-scale, long-period atmospheric waves such as tides [e.g., *Hines*, 1968; *Taylor and Edwards*, 1991].

Usually, gravity waves are measured as the superposition of waves with various frequencies and wavelengths, and thus it is necessary to use various techniques to measure them since each technique has limitations in both time and height resolution [*Nakamura et al.*, 1996]. In optical methods such as all-sky cameras (ASC), which measure airglow emission arising from various constituent layers such as the NIR OH (peak altitude ~87 km), Na (589.2 nm) (peak altitude ~90 km) and OI (557.7 nm) (peak altitude ~96 km) emission, gravity waves with horizontal scales up to a few hundred km [e.g., *Taylor et al.*, 1995d; *Swenson et al.*, 1995; *Wu and Killeen*, 1996] are easily measured. Photographic studies of noctilucent clouds (base altitude ~83 km) have also been used in some optical studies of gravity waves [e.g., *Haurwitz and Fogle*, 1969]. Radar observations have also been made at various locations to investigate the spectral contents of gravity waves such as their frequency and vertical wavenumber [e.g., *Frezal et al.*, 1981; *Carter and Balsley*, 1982; *Vincent*, 1984; *Meek et al.*, 1985; *Reid*, 1986; *Nakamura et al.*, 1996]. One of the most useful radar instruments to investigate gravity wave energy deposition in the mesosphere and the associated height profiles of the upward flux of horizontal momentum is the mesosphere-stratosphere-troposphere (MST) radar [*Nakamura et al.*, 1996]. MST radars have good time and height resolution and have the ability to observe continuously, but their height coverage is limited to two specific regions below 25 km and 60 to 90 km [e.g., *Shibata et al.*, 1988; *Wilson et al.*, 1990, 1991]. In comparison, Na lidar techniques provide one of the best methods for

measuring the vertical structure of such waves in the 80 to 100 km region [e.g., *Gardner and Voelz*, 1987], whereas Rayleigh lidars can be used to measure the temperature and density fluctuations in the 30 to 80 km altitude range [e.g., *Chanin and Hauchecorne*, 1981; *Shibata et al.*, 1988; *Wilson et al.*, 1990, 1991]. The limitations of Na lidar systems come from the spatial and temporal resolution caused by photon noise [e.g., *Gardner and Voelz*, 1987]. Improvements in Rayleigh scatter lidar systems now allow the study of the vertical wavenumber and temporal frequency spectra of gravity wave-induced winds as well [e.g., *Chanin*, 1986; *Shibata et al.*, 1986]. Those obtained by in situ measurement such as radiosondes and rocketsondes provide "snap-shot" profiles of winds, temperature, and pressure below ~35 km altitude and between 20 to 60 km, respectively [e.g., *Hirota and Niki*, 1985; *Kitamura and Hirota*, 1989; *Tsuda et al.*, 1991, 1994; *Murayama et al.*, 1992].

1.3.2 Theory of Gravity Waves

One dimension is enough to describe a sound wave since its motion is longitudinal. In the case of gravity waves, the oscillations are transverse to the direction of propagation, and three dimensions are needed to describe them. However, to obtain a simple solution to the fundamental equation for the gravity waves we can (1) treat gravity waves in two dimensions only (where x is in the direction of propagation, and z is transverse to the x direction), (2) ignore the Coriolis term since the horizontal scale of the gravity wave of interest is much smaller than tides and planetary waves, (3) neglect friction and dissipation, and (4) assume an isothermal stationary atmosphere. Using the

momentum equation, the continuity equation, and the law of conservation of energy, we can assume small wave-like perturbations of the form:

$$\exp(\alpha z) \exp i(\omega t + kx + mz) \quad (1-8)$$

where the first exponential represents the variation of wave amplitude with altitude, ω is the angular wave frequency, m is the vertical wave number ($= 2\pi / \lambda_z$), k is the horizontal wave number ($= 2\pi / \lambda_x$), and λ_x and λ_z are horizontal and vertical wave components of the gravity wave. Solving for internal waves (i.e., $m \neq 0$), we get the following dispersion relations [Hines, 1960]:

$$\omega^4 - \omega^2 C^2 (k_x^2 + k_z^2) + (\gamma - 1)g^2 k_x^2 - \omega^2 \gamma^2 g^2 / 4C^2 = 0 \quad (1-9)$$

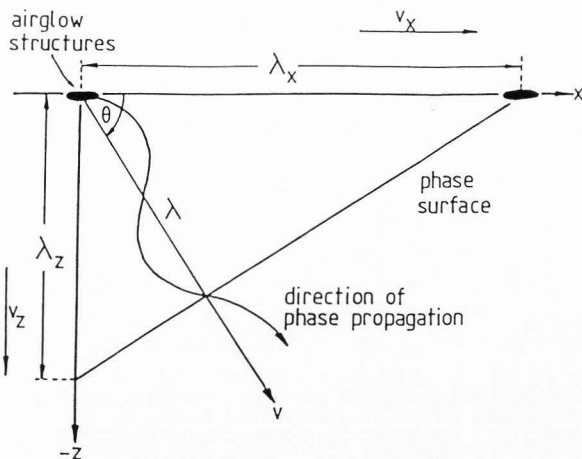
where ω : angular frequency

γ : the ratio of specific heats of the atmospheric gas

C : the speed of sound

g : the acceleration due to gravity

Full details on the procedure of this derivation are given in the Appendix. Figure 1.7 illustrates the relationships between the vertical and horizontal gravity wave parameters as described by Hargreaves [1979].



$$k = \frac{2\pi}{\lambda} ; \quad v = \frac{\lambda}{T} ; \quad \tan \theta = \frac{\lambda_x}{\lambda_z} ; \quad \frac{1}{\lambda^2} = \frac{1}{\lambda_x^2} + \frac{1}{\lambda_z^2}$$

Figure 1.7 Relationship between wavelength, velocity, and propagation angle [Hargreaves, 1979].

$$\theta = \tan^{-1}(\lambda_x / \lambda_z) = \tan^{-1}(k_z / k_x) \quad (1-10)$$

$$1 / \lambda^2 = 1 / \lambda_x^2 + 1 / \lambda_z^2 = (k_x^2 + k_z^2) / (2\pi)^2 \quad (1-11)$$

$$\lambda = 2\pi / (k_x^2 + k_z^2)^{1/2} \quad (1-12)$$

$$v = \omega \lambda / 2\pi = \omega / k \quad (1-13)$$

$$v_x = \omega / k_x \quad (1-14)$$

$$v_z = \omega / k_z \quad (1-15)$$

When $g = 0$, i.e., for a pure sound wave, the dispersion relation becomes:

$$C = \omega / (k_x^2 + k_z^2)^{1/2} = \omega / k = \omega \lambda / 2\pi = \lambda / \tau \quad (1-15)$$

where τ is the wave period. When $\omega_a^2 / k_x^2 \ll C^2$, that is, removing the effect of compressibility, the dispersion relation for a pure gravity wave becomes:

$$k_z^2 = k_x^2 (\omega_B^2 / \omega^2 - 1) \quad (1-16)$$

And the phase propagation angle becomes:

$$\theta = \tan^{-1} (\omega_B^2 / \omega^2 - 1)^{1/2} \quad (1-17)$$

where $\omega_a = \gamma g / 2C$ is termed the acoustic cut-off frequency and

$\omega_B = (\gamma - 1)^{1/2} g / C$ is the Brunt-Vaisala frequency.

Figure 1.8 shows dispersion curves for an AGW showing the acoustic and the gravity wave regions. The wave can only propagate if k_x and k_z are real and positive, requiring that $\omega < \omega_B$. In fact, the negative square root of equation (1-18) should be taken, because the phase progression angle for a pure gravity wave is directed downwards for upward energy propagation [Hargreaves, 1979]. Figure 1.9 shows contours of constant period in the k_x - k_z domain as derived by Hines [1960].

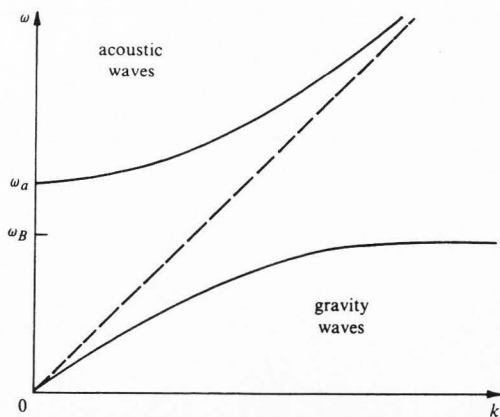


Figure 1.8 Dispersion curves for an AGW showing the acoustic and the gravity wave regions [Houghton, 1989]. Note the forbidden region where $\omega_B < \omega < \omega_a$.

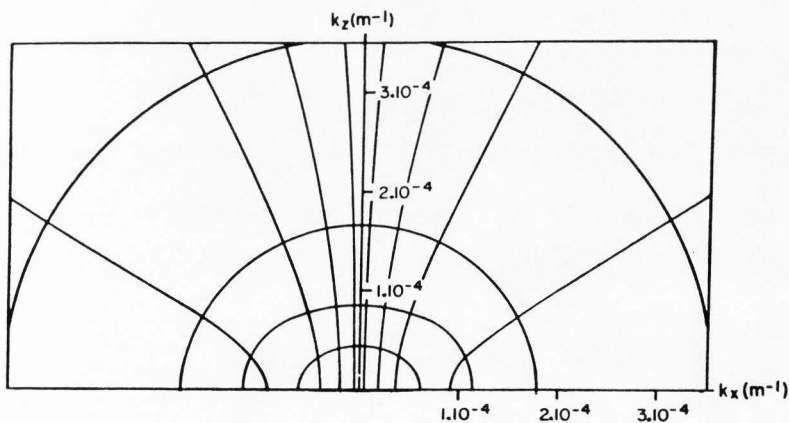


Figure 1.9 Contours of constant period in the k_x - k_z domain adapted from Hines [1960].

1.3.3 Properties of Gravity Waves

Figure 1.10 illustrates a simple gravity wave. At the lowest frequencies (i.e., longest periods) the direction of the air particles is perpendicular to the direction of phase progression. "In an acoustic wave the nature of the medium determines its velocity, so that the wavelength is fixed by selection of a frequency through not the direction of propagation. In the case of gravity waves, the propagation angle is determined by selection of the frequency not by the velocity or the wavelength" [Hargreaves, 1979, p. 131]. Usually the observed phase speed of short period gravity waves is much slower than the speed of sound and typically $<100 \text{ ms}^{-1}$ [e.g., Taylor *et al.*, 1987].

Reid [1986] has shown that high-frequency saturating and/or dissipating gravity

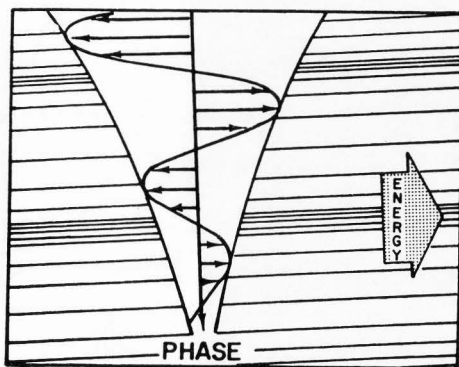


Figure 1.10 Pictorial representation of an internal atmospheric gravity wave [Hines, 1960]. Note the increasing amplitude with height and the downward phase propagation for upward phase directed energy flow (the group and phase speeds are orthogonal for a pure gravity wave).

waves are the main source of mean flow acceleration. Higher frequency waves propagate more vertically, whereas very long period waves propagate essentially horizontally. Figure 1.11 illustrates this relationship [Hines, 1967]. Lower frequency waves generated in the troposphere must travel much longer distances before they achieve mesospheric altitude and thus may suffer more from filtering, refraction, and dissipation effects than short period waves [Reid, 1986]. Because of a saturation of upward propagating gravity waves, the vertical scales of dominant gravity waves increase with altitude [Tsuda *et al.*, 1994].

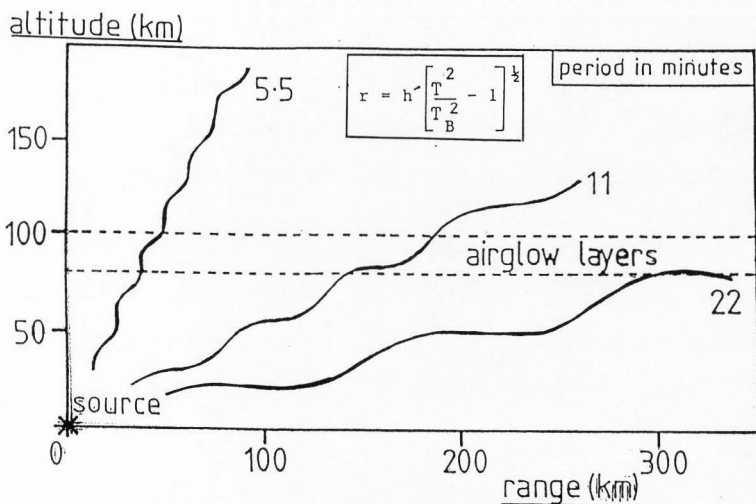


Figure 1.11 Propagation characteristics of gravity waves into the upper atmosphere adapted from Hines [1967].

In a recent study of small-scale mesospheric gravity waves using OH image data, a strong dependency on season was found with the highest wave occurrence in the summer months and lowest occurrence in the winter months [Wu and Killeen, 1996]. The sources and propagation directions of mesospheric gravity waves can in principle be identified by the latitudinal variations of the gravity wave energy and momentum flux [Nakamura *et al.*, 1996], or by ray tracing techniques, but studies of sources are still relatively rare [e.g., Taylor and Hapgood, 1988].

1.4 Thesis Topic

In this thesis I have focused attention on short period (<1 hour) internal atmospheric gravity waves, especially the phenomenon of "frontal events," which were recently discovered in the MLT region using all-sky image measurements [Taylor *et al.*, 1995e]. The purpose of this thesis is to investigate the characteristics of these frontal events and to compare their properties with a new theory on mesospheric "undular bores" based on similar morphology phenomena observed in the lower atmosphere (called morning glory) and on some rivers (termed river bores). I have used extensive image data obtained using an all-sky Charged Coupled Device (CCD) camera operated from the Bear Lake Observatory (BLO), Utah (41.6°N, 111.6°W, 1990 m) during the past four years (1994 to 1997). These measurements are continuing but have so far yielded 16 examples of mid-latitude frontal events for this study.

CHAPTER 2

IMAGING GRAVITY WAVES

2.1 Review of Gravity Wave Imaging

Several imaging techniques for measuring small-scale (<100 km horizontal wavelength), short-period (<1 hour) gravity waves in the MLT region have been developed over the past 25 years. The initial image data were provided by long exposure (~10-15 min), near infrared (NIR) photographic cameras. These were subsequently replaced by intensified video cameras providing much shorter exposure times (typically a few seconds) but limited spatial resolution. These in turn have now been superseded by solid-state digital imaging systems of high resolution (e.g., 1024 x 1024 pixels) and high sensitivity at visible and NIR wavelengths [e.g., *Swenson and Mende*, 1994; *Taylor et al.*, 1995a; *Wu and Killeen*, 1996].

Early photometric observations of the nightglow emission layers showed that they often displayed irregularities, called "structure" [e.g., *Kieffaber*, 1973]. In most cases this structure seemed patchy and erratic but sometimes it exhibited well ordered, wave-like motions particularly in the NIR OH emission [*Peterson and Kieffaber*, 1973]. Today we now know that many of these wave motions are due to the passage of short-period internal gravity waves through the emission layers [e.g., *Taylor and Hapgood*, 1988].

Taylor [1997] has recently summarized several "milestone" papers describing observations of various nightglow emissions and their importance for investigating the properties of these wave motions. In particular, improvements in sensitivity of the

imaging systems used for these studies over the past 25 years have resulted in a deeper understanding of small-scale gravity wave occurrence, propagation, and dissipation at MLT heights.

Because of the nature of the early “single point” photometric measurements, it was often difficult to know whether the structure evident in the nightglow emissions was due to spatial or temporal changes. In an effort to solve this problem, *Peterson and Kieffaber* [1973] made the first photographic observations of OH structure using the (then) recently developed Eastman Kodak high-speed infrared film and a 35-mm still camera. A copy of one of their early photographs showing “cloud-like” structure (as they termed it) is presented in Figure 2.1 The picture was obtained using an ~10 min exposure and was filtered to observe the sub-micron wavelength range (740-900 nm), which is dominated by several OH Meinel bands (see Figure 1.3).

Subsequently, *Moreels and Herse* [1977] used an array of four narrow field (40° each) photographic cameras (which were similar to those used by Peterson and

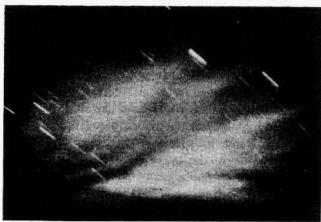


Figure 2.1 Long exposure, near infrared photograph showing “cloud-like” OH structures at ~15° elevations over New Mexico [*Peterson and Kieffaber*, 1973].

Kieffaber) arranged with overlapping fields of view to observe a much larger fraction of the low-elevation sky. Their work confirmed the existence of NIR OH structure but most frequently in the form of extensive wave-like patterns, which they speculated were probably due to gravity waves. Later, *Armstrong* [1986] used image-intensified film to perform the first classification of the wave patterns into groups according to their appearance and horizontal scale sizes, while *Clairemidi et al.* [1985] obtained novel images of wave structure at high latitudes (and in presence of aurora) and concluded that nightglow wave structures are a global phenomenon and can occur at any latitude.

In parallel with the developments in photographic techniques, *Crawford et al.* [1975] developed a low-light TV system (originally used for medical scanning) to obtain the first high temporal resolution (1/7 sec exposure) "real-time" images of NIR wave structure. Using a similar type TV system, *Taylor et al.* [1987] observed an unusual wave display, called a "bright night" in the visible wavelength OI (557.7 nm), Na (589.2 nm), and the broad band (710-850 nm) NIR OH emission. Similar short-period (~12 min) wave patterns were observed in each of these emissions, which led *Taylor et al.* to conclude that the perturbing gravity wave was most probably freely propagating throughout the MLT region (~80-100 km). In a related paper they subsequently determined that the most likely source of the waves was an isolated thunderstorm [*Taylor and Hapgood*, 1988].

With the commercial availability of sensitive, solid-state (CCD) detectors in the early 1990's, significant advantages over existing video systems for quantitative intensity measurements of the two-dimensional wave field were made. Figure 2.2

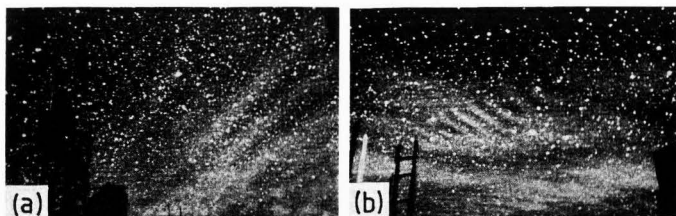


Figure 2.2 Two narrow field CCD images, showing (a) “bands” and (b) “ripples” imaged in the near infrared OH emission from Haleakala Crater, Maui, HI, during the ALOHA-90 campaign [Taylor and Hill, 1991].

shows two narrow field images of NIR wave structure obtained using a high-performance, low-noise, bare CCD imager (originally developed for astronomical studies). The measurements were made from a high-altitude site on the Hawaiian Islands during the ALOHA-90 (Airborne Lidar Observations of the Hawaiian Airglow) campaign [Taylor and Hill, 1991]. Two types of wave structures termed “bands” and “ripples” are evident (these will be discussed more detail in section 2.3).

Peterson and Adams [1983] obtained the first “fish-eye” (180° field of view) images showing wave structure over the whole sky (covering more than $\sim 0.5 \times 10^6$ km² at mesospheric heights) using an intensified photographic camera and exposure times of 3 and 10 sec. These events were considered rare until Taylor *et al.* [1993] used a low-light TV system (capable of integrating the image signal for several seconds) to measure all-sky images of OH structure on an almost nightly basis from Colorado during the MAPSTAR (Middle Atmosphere Periodic Structure and Associated Radiance) campaign [Taylor *et al.*, 1993].

There then followed a series of successful attempts to image OH wave structure over large areas of sky, using sensitive, low-noise, CCD detectors. In particular *Swenson and Mende* [1994] obtained high-contrast images of all-sky structure using a broad-band filter arrangement (750-930 nm) while *Hecht et al.* [1994] investigated intensities and rotational temperatures of the NIR OH (6,2) band and the O₂ (0,1) band emissions over a limited field of view (~60°) centered on the zenith by using a set of narrow band filters. In contrast, the properties of somewhat longer period gravity waves have been investigated successfully using a novel imaging system (MORTI: Mesospheric Oxygen Rotational Temperature Imager) developed to measure the intensity and rotational temperature of the O₂ (0,1) band emission simultaneously at many points in a ring on the sky [e.g., *Wiens et al.*, 1995].

Today the quantitative capabilities of the CCD imager are used regularly for wide-field, monochromatic measurements of the visible and NIR nightglow emissions using broad and narrow band optical arrangements [e.g., *Swenson et al.*, 1995; *Taylor et al.*, 1995 a, b, c, d; *Wu and Killeen*, 1996]. Figure 2.3 shows an example of all-sky wave structure imaged in the NIR OH emission during the ALOHA-93 campaign [*Swenson et al.*, 1995]. The data were obtained from an aircraft flying over the Pacific Ocean and in this example the wave structure is highlighted by subtracting two consecutive images to create a "difference image." The extensive nature of the short horizontal wavelength (~14 km) wave pattern is clearly evident.

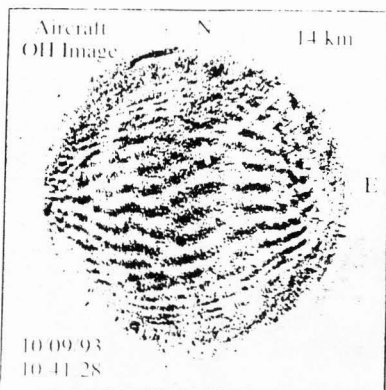


Figure 2.3 All sky “difference image” showing a coherent wave pattern recorded in the NIR OH emission during the ALOHA-93 campaign. The observations were made from an aircraft flying over the Pacific Ocean to extend the geographical coverage of the measurements [Swenson *et al.*, 1995].

2.2 The Utah State University All-Sky Nightglow Imager

A large area (6.45 cm^2) solid-state charged coupled device (CCD), consisting of 1024×1024 pixel array thermoelectrically cooled to operate at -40° C , was used to obtain high-quality image data on gravity waves. Figure 2.4 shows a schematic diagram of the imager as developed in 1993. A characteristic of the CCD device is its high quantum efficiency ($\sim 80\%$ at visible and 50% at NIR wavelengths) and low-noise (dark current $< 0.5 \text{ e}^- / \text{pixel} / \text{s}$), which makes it very suitable for quantitative measurements of faint, low contrast ($< 5\%$) gravity wave signatures in the visible and NIR nightglow emissions. The camera is equipped with a fast ($f/4$) telecentric lens system and a five-

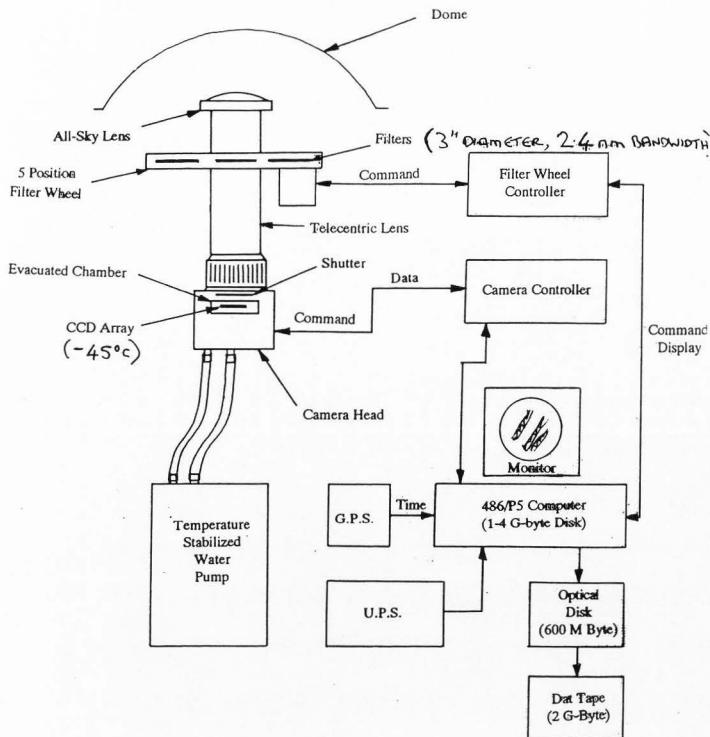


Figure 2.4 Schematic diagram showing the USU all-sky CCD imager developed in 1993 by M.J. Taylor.

position, temperature-stabilized filter wheel which provided all-sky (180°) coverage using 3-inch diameter, high transmission (~75 %) interference filters. The measurements presented in this thesis were obtained from Bear Lake Observatory, UT (see Chapter 4) and consist mainly of observations of the NIR OH, Na (589.2 nm), and OI (557.7 nm)

Table 2.1 Characteristics of the Filters Used for the All-Sky Nightglow Measurements

Filter / Height	Wavelength (nm)	Bandwidth (nm)	Transmission (%)	Integration Time (sec)
OI (96 km)	557.7	2.65	~ 83	90
Na (90 km)	589.2	2.5	~ 80	120
Bg	572.5	2.67	~ 83	90
OH (87 km)	715 - 1000	(O ₂ notch)	~ 80	20

MLT emissions. The characteristics of the filters used for these MLT measurements presented here are listed in Table 2.1. In addition to these measurements, a series of background (Bg) images was obtained to help distinguish tropospheric cloud in the data and to aid detailed spectral analyses (not discussed here).

Observations of the nightglow emissions were recorded typically once every ~9 min for the Na and Bg images and every 4 to 5 min for the OH and the OI (557.7 nm) emissions. Data were recorded onto DAT tape and transferred to optical disk for analysis in the laboratory.

2.3 Types of Short Period Gravity Waves

As mentioned previously, several researchers have attempted to classify their observations of short-period (<1 hour) gravity waves often into different groups [e.g., *Clairemidi et al.*, 1985; *Armstrong*, 1986; *Taylor*, 1986b]. A consistent result indicates that there are two types of short-period waves termed "bands" and "ripples" which have distinct spatial and temporal properties [e.g., *Taylor et al.*, 1997].

2.3.1 Bands

Bands are the most prominent group, usually appearing as an extensive series of quasi-monochromatic waves that exhibit horizontal wavelengths of a few to several tens of kilometers. Bands are persistent and can endure typically for a few to several hours (sometimes limited by the available observation time) but the same pattern is not usually seen on successive nights [e.g., *Taylor and Hill*, 1991]. Some studies have shown that this type of wave pattern is associated with the passage of freely propagating (or ducted) gravity waves, which probably originate from the troposphere [e.g., *Taylor and Hapgood*, 1988; *Isler et al.*, 1998]. According to recent measurements, band-type gravity waves are as prevalent over oceans as they are over continental mountainous regions, which suggests their most likely sources are convective weather disturbances rather than orographic forcing by winds blowing over mountains [e.g., *Taylor and Hill*, 1991; *Swenson et al.*, 1995; *Taylor et al.*, 1995a]. Bands usually exhibit phase speeds up to 100 ms^{-1} (typically $20\text{-}70 \text{ ms}^{-1}$) resulting in observed wave periods of typically 10 to 20 min (maximum ~ 1 hour).

2.3.2 Ripples

Ripples have quite different properties from bands: they are much smaller in spatial extension (typically $< 5 \times 10^3 \text{ km}^2$) and exhibit considerably shorter lifetimes (< 45 min) [e.g., *Peterson*, 1979]. Their wavelength range is typically 5 to 15 km and their observed periods cluster around 5 min [*Taylor et al.*, 1997]. These properties suggest that ripples may result from localized regions of strong wind shear, which in turn generate small-scale waves in situ through the Kelvin-Helmholtz instability [e.g.,

Haurwitz and Fogle, 1969; Taylor and Hapgood, 1990. One source for the ripples may result from the chance combination of wind and wave motions (of tidal or other origin) creating temporary large amplitude waves and an associated shear instability. However, *Fritts et al. [1993]* and *Hecht et al. [1997]* have proposed an alternative convective-type instability mechanism as a possible source of some of the smaller scale, shorter lived waves.

CHAPTER 3

“FRONTAL EVENTS”

3.1 Introduction

During the ALOHA-93 campaign, a suite of airborne and ground-based optical instruments was operated from Maui, Hawaii, to investigate the dynamics and sources of short-period gravity waves over a low latitude (20.8°N, 156.2°W) oceanic site [e.g., Gardner, 1995; Taylor *et al.*, 1995a]. These instruments included the University of Western Ontario infrared Michelson Interferometer (UWOMI-3) and the (then) recently developed multi-wavelength, all-sky CCD imager of Utah State University. During this campaign many extensive band and transient ripple events were measured in the four nightglow emissions imaged: OI (557.7 nm), OH, Na (589.2 nm), and O₂ atmospheric band (0,1).

However, on 10 October, a most unusual wave event was observed. This disturbance appeared as a leading sharp “front” followed by several conspicuous wave crests which progressed coherently across the sky from horizon to horizon (~900 km at MLT altitude).

As the “front” passed overhead, the co-aligned Michelson Interferometer (10° field of view) detected a sudden increase in the OH M (3,1) band intensity and its rotational temperature (with the temperature increase apparently leading the intensity change by almost 15 min). At the same time the imager registered a sharp decrease in the OI (557.7 nm) emission intensity. A description of this unusual event was reported by Taylor *et al.* [1995e] in a paper entitled “Spectrometric and Imaging Measurements of a

Spectacular Gravity Wave Event" as part of a special issue of *Geophysical Research Letters* (GRL) covering the ALOHA-93 campaign.

This thesis concerns the detection and measurement of similar type wave displays, which we now term as a "frontal events" in the all-sky image data recorded from our mid-latitude observatory at Bear Lake (BLO). The data were obtained over the past four years using the same camera system and the same integration times as determined for the Hawaiian measurements. Sixteen total displays have been identified as good candidates for frontal events, suggesting that their occurrence is quiet rare. Also as will become apparent later, their visual characteristics varied considerably. Before presenting the result of this study, it is pertinent to summarize first the novel observations of *Taylor et al.* [1995e] to provide a background comparison.

3.2 Summary of ALOHA-93 Front-Like Data

3.2.1 Description of Image Data

Figure 3.1 shows a sequence of all sky images illustrating the unusual morphology of this event and its transit through the Hawaiian sky as recorded in the NIR OH and the OI (557.7 nm) nightglow emission. This event was first detected around 09:30 UT in the northwestern sky near the limit of the camera's field of view (~450 km range). The disturbance was peculiar as it appeared bright in the OH and Na emissions but dark in the OI and O₂ emissions (suggesting a reversal in contrast of the wave pattern for the lower altitude OH and Na emissions versus the higher altitude OI and O₂ layers).

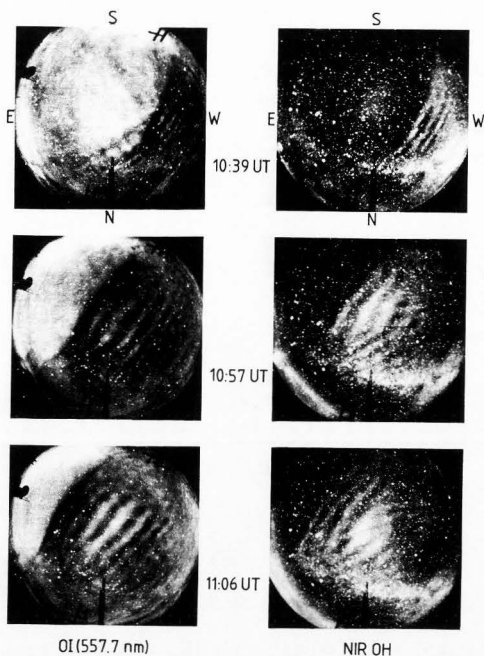


Figure 3.1 Sequence of all-sky CCD images showing OI (557.7nm) (left) and NIR OH (right) (integration time for OI = 90 s, OH = 20 s). Note the reversal in contrast of the structures in the two emissions images [Taylor *et al.*, 1995e].

Over the next hour the disturbance was clearly resolved as a series of elongated wave crests characterized by a sharp leading “front” propagating rapidly towards the southeast. The front passed overhead at the observing site (Haleakala crater, Maui) at approximately 10:50 UT. Some 40 min later the disturbance had progressed well to the southeast of Maui and only faint evidence of its passage remained in the zenith sky.

Throughout this time the wave pattern remained temporally coherent in each of the four emissions observed and exhibited several spatially extensive wave crests (effectively extending across the entire camera field).

3.2.2 Measurements of Wave Parameters

Figure 3.2 and 3.3 illustrates the geographic location, orientation, and motion of the frontal event as observed in the OI (557.7 nm) emission. The data are plotted for an assumed emission altitude of 96 km. Analyses of these data yielded a horizontal wavelength ($\lambda_x \sim 19$ km) and horizontal phase speed ($v_x \sim 76$ ms⁻¹) indicating a very short observed period (τ_{ob}) of approximately 4.2 min, close to the local Brunt-Vaisala period. Wind measurement from an MF radar located at Kauai (at ~ 375 km range) during this event indicates relatively low wind speeds of only a few meters per second in the direction of the motion of the wave, suggesting that the intrinsic period of this event was very close to its observed period [Taylor *et al.*, 1995e].

Within the limits of the measurements, all four emissions indicated identical wave parameters establishing that the disturbance extended coherently throughout the MLT region (~ 80 -100 km). Spatial measurements also showed that the front exhibited no observable phase shift between the OH and OI structure consistent with a ducted or evanescent wave motion and a period of approximately 5 min [Isler *et al.*, 1998]. A summary of the observed wave parameters for each of the nightglow emissions is given in Table 3.1.

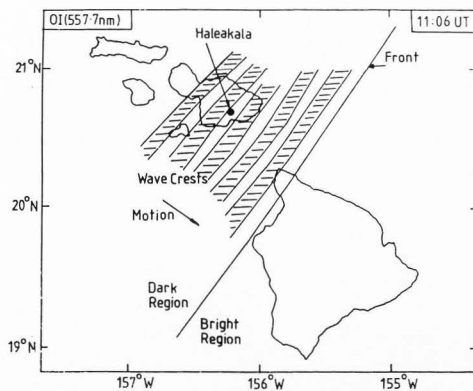


Figure 3.2 Ground map showing the geographic location and orientation of the OI wave pattern at 11:06 UT shortly after the front passed overhead.

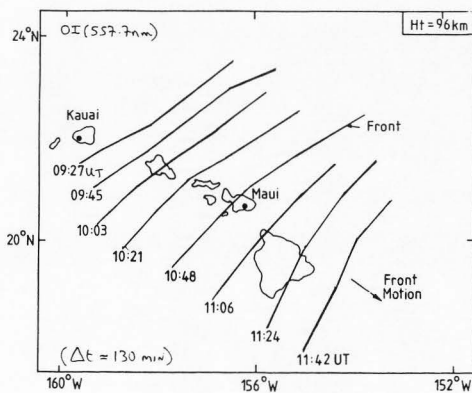


Figure 3.3 Map showing the orientation and motion of the OI wave front as it passed first over Kauai, Maui, and then Big Island during 130-min period.

Table 3.1 Horizontal Wave Parameters of the Four Nightglow Emissions Recorded on 10 Oct. 1993 During the ALOHA-93 Campaign [Taylor *et al.*, 1995e]

Emission	Assumed Height (km)	λ_h (km)	v_h (ms ⁻¹)	T_{obs} (min)
OH	87	19.3 ± 0.7	75 ± 2	4.3 ± 0.2
Na	90	18.8 ± 0.7	77 ± 2	4.1 ± 0.2
O ₂	94	18.8 ± 0.9	76 ± 3	4.1 ± 0.3
OI	96	20.1 ± 0.7	77 ± 2	4.4 ± 0.2
Average		19.3 ± 0.7	76 ± 2	4.2 ± 0.2

3.2.3 Relative Intensity Measurements

As already mentioned, an extraordinary characteristic of this event was the apparent reversal in contrast between the structures imaged in the OH emission (peak height ~87 km) compared with those recorded in the OI (557.7 nm) emission layer (peak height ~96 km). Specifically, at OH wavelength the frontal event exhibited a set of "bright" wave crests propagating through a "dark" structureless sky while at the same time in the OI emission the front propagated into a "bright" nightglow region leaving an apparently depleted emission in its wake. Figure 3.4 shows a relative intensity measurement of these two emissions recorded as the wave passed through the zenith at 10:57 UT. Each scan was made across the central two thirds of the camera field of view in a direction normal to the wave crests. For clarity, the data have been flat-fielded to remove the competing effects of line-of-sight integration through the nightglow layers and lens vignetting. The step-like or frontal nature of the event is clearly evident. Relative intensity measurements indicate a significant increase of approximately 33 % in

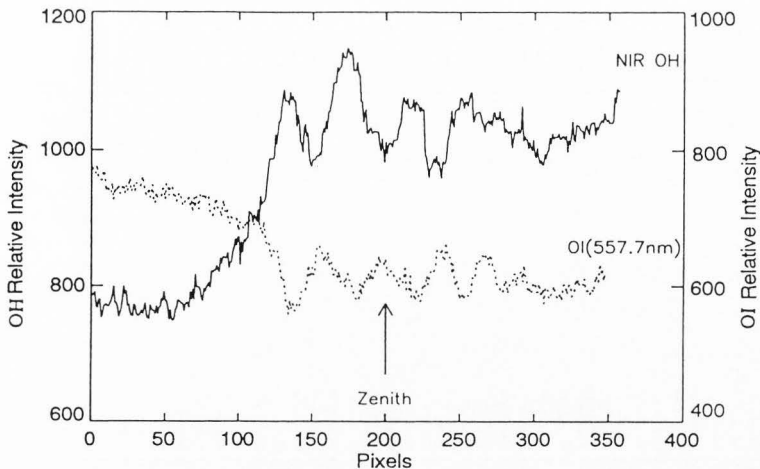


Figure 3.4 Relative intensity plot normal to the wave crests for the OH and OI data at zenith. Solid and dotted plots indicate NIR OH and OI emission, respectively [Taylor *et al.*, 1995e].

the NIR OH signal and a corresponding decrease of 24% in the OI signal at this time. In comparison, the amplitude of the waves trailing the front varied from approximately 8 to 16%. A similar, but less contrasted, effect was observed in the Na and O₂ emissions with the Na images exhibiting similar appearance to the OH data while the O₂ images paralleled the OI data.

As will be discussed later (Chapter 6), both the front-like nature of this event and the observed contrast reversal may be explained by the passage of a ducted “bore-like” intrusion through the MLT region [Dewan and Picard, 1998]. This explanation was first postulated by Dewan [private communication] shortly after the publication of the

Taylor et al. [1995e] paper.

3.2.4 Summary of ALOHA-93 Event Characteristics

The following list describes the most pertinent characteristics of this wave event:

- 1) unusual "front-like" morphology
- 2) sharp change in intensity induced by the passage of the front
- 3) high apparent phase speed ($\sim 76 \text{ ms}^{-1}$)
- 4) short observed and intrinsic periods ($< \sim 5 \text{ min}$)
- 5) coherent wave progression from horizon to horizon
- 6) same disturbances present in all four emissions
- 7) contrast reversal in OH and OI wave structure.

In addition to these characteristics, the Michelson interferometer observed a significant increase in rotational temperature ($\sim 20 \text{ K}$) associated with the passage of the front. In the following chapters, these characteristics have been used to help identify similar-type events in the all-sky image data recorded at BLO. Unfortunately, coincident interferometer/temperature data are not readily available for comparison.

CHAPTER 4

MID-LATITUDE MEASUREMENTS OF "FRONTAL EVENTS"

4.1 Bear Lake Observatory

Bear Lake Observatory (BLO) is located in the Wasatch Mountain range, Utah (41.9° N 111.4° W, 1990 m) about 61 km by road (38 km line of sight) from Utah State University, Logan, Utah. It can be reached easily by car (~1 hour) along US highway 89. Figure 4.1 shows a view of the observatory overlooking Bear Lake. Utah State University (USU) donated the main observatory building (a 20 x 4 m² portable office trailer), which is securely surrounded by a chain linked and barbed wired fence on a 60 x 60 m² site. The main observatory building consists of seven 1.8 x 1.8 m² experiment stalls and a radar room that is shielded against electromagnetic radiation. Each stall has two independent 15 A, 110 V, 60 Hz AC circuits (which may be combined to provide 220 V if required). Several dedicated telephone lines are available for voice and data communication. First detailed measurements of the night sky were made from BLO in 1990/91 in coordination with the Upper Atmosphere Research Satellite (UARS).

In 1992, USU sponsored a refurbishment, which included a kitchen, a loading dock, a toilet, and a covered stairway to the roof. The roof over the experiment stalls was also modified for easy access to the experiment domes. A variety of domes designed to satisfy the requirements of various instruments of differing fields-of-view, look angles and wavelengths (UV to IR) is available.

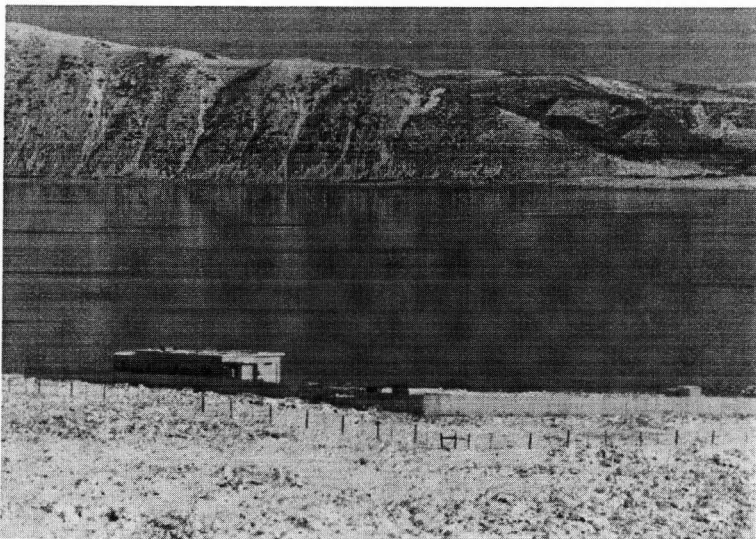


Figure 4.1 Bear Lake Observatory, Utah (courtesy V. Wickwar).

BLO is located on the east side of the mountain range in the rain-shadow. The air is clear because of relatively high altitude and rural location, and there is minimal scattered light. Thus it provides excellent optical observing conditions. There are about 200 clear nights a year, and the best observing season is June to October. The all-sky camera used for these measurements resides in one of the stalls at BLO and is operated each month for ~15 days centered on the new moon. (Due to campaign measurements at other sites, data have not been obtained continuously.) Nevertheless, an excellent ensemble of data has been obtained covering all seasons over the past four years.

4.2 Image Analysis

To investigate the occurrence and properties of frontal events, I first examined the available BLO data set using a purpose-built browse program designed to give rapid viewing of the data. In this way, I have identified 16 clear signatures of frontal events from 29 months data. These events were then analyzed to determine the horizontal parameters of the wave motions: horizontal wavelengths, phase speeds, and directions of motion. The images were calibrated first using the star background to determine the elevation and azimuth of any point in the image field. (The typical accuracy of this calibration is to within 1 pixel, equivalent to ~ 20 arc min.) A description of this procedure, as applied to a narrow angle data, is given by *Hapgood and Taylor* [1982]. Each pixel in the CCD array subtends an equal angle on the sky resulting in an almost linear relationship between zenith angle and distance as measured from the center of the image. To correct for geometrical distortion arising from nonparallel lines of sight in the image itself (due to the all-sky lens format), the outlines of prominent wave crests in each image were traced and mapped onto the ground, assuming a centroid emission altitude of 87 km for the OH emission [*Baker and Stair*, 1988], 90 km for the Na emission [*Green and Best*, 1967], and 96 km for the OI (557.7 nm) emissions [*Offermann and Drescher*, 1973]. For each wave event, measurements from a time series of images (and maps) were used to determine the mean horizontal wavelength, observed phase speed (and hence observed period), predominant direction of motion (usually to within an accuracy of $\pm 5^\circ$), and induced intensity modulation. The results of this analysis are given in Chapter 5 (see Table 5.1 and Table 5.2).

4.3 Criteria for Identifying Frontal Events

According to *Taylor et al.* [1995e], there are several methods to distinguish frontal events from other band-like wave displays. Especially among them I applied the following rules to the Bear Lake data set.

- (1) The image data should exhibit a sharp leading front and an associated step-like change in intensity induced by the passage of the front.
- (2) There should be a limited number (typically <10) of associated waves trailing the front.
- (3) The front should be evident in both the OI and OH data (but this was not always the case).
- (4) There should be evidence for a contrast reversal between the OI and OH data.
(As will be discussed later, this was found not to be a necessary feature.)

4.4 Examples of Bear Lake Frontal Events

The following six examples illustrate clear frontal event characteristics chosen from a total of 16 events identified (so far) in the Bear Lake data set.

4.4.1 21 January 1994

A beautiful but relatively faint example of a frontal event was observed in all three MLT emissions (OH, Na, OI) measured. It first appeared at ~11:40 UT in the northern sky, passed through the zenith at ~12:47 UT, and the number of trailing waves was observed to increase with time from ~11:40 to ~13:30 UT. The duration of the observations was limited by sunrise at ~13:30 UT. Figure 4.2 shows this event as

imaged in all three nightglow emissions at two times separated by ~ 20 min, around 12:50 and 13:10 UT. The motion of the front and associated waves is clearly evident. It is also immediately evident that, in this case, there is no contrast reversal in the images of this pattern in each emission layer due to the passage of front. The wave pattern extended over the whole sky and exhibited a horizontal velocity of $\sim 55 \text{ ms}^{-1}$, an average horizontal wavelength of ~ 22 km yielding an average observed period of ~ 6.6 min. The observed direction of motion was $\sim 184^\circ$ (i.e., approximately due southward).

4.4.2 4 May 1994 (two frontal events)

The first frontal event appeared at $\sim 05:05$ UT in the low elevation northwestern sky and was most evident in the NIR OH and OI (557.7 nm) emission layer. It passed through the zenith at $\sim 05:54$ UT, and the number of companion waves was observed to increase from 3 to 4 (possibly 5) crests during a 40-min period. This is illustrated in the series of OH images shown in Figure 4.3. In this event, a clear contrast reversal between the NIR OH and OI (557.7 nm) emissions was observed, which is evident in Figure 4.4, which shows two OI images during the same period. The OI (557.7 nm) data show wave propagation into a comparatively bright airglow region while the OH wave motion progressed into an apparently dark structureless sky. This event is therefore similar in many respects to the ALOHA-93 frontal event. The waves were observed to extend over \sim two-thirds of the sky and to propagate rapidly with a horizontal phase speed of $\sim 68 \text{ ms}^{-1}$ (at an azimuth of $\sim 130^\circ$ i.e., towards the southeast). However, the average horizontal wavelength was only ~ 11 km, indicating a very short observed wave period of ~ 2.8 min less than the Brunt period and suggestive wind effects in the MLT region.

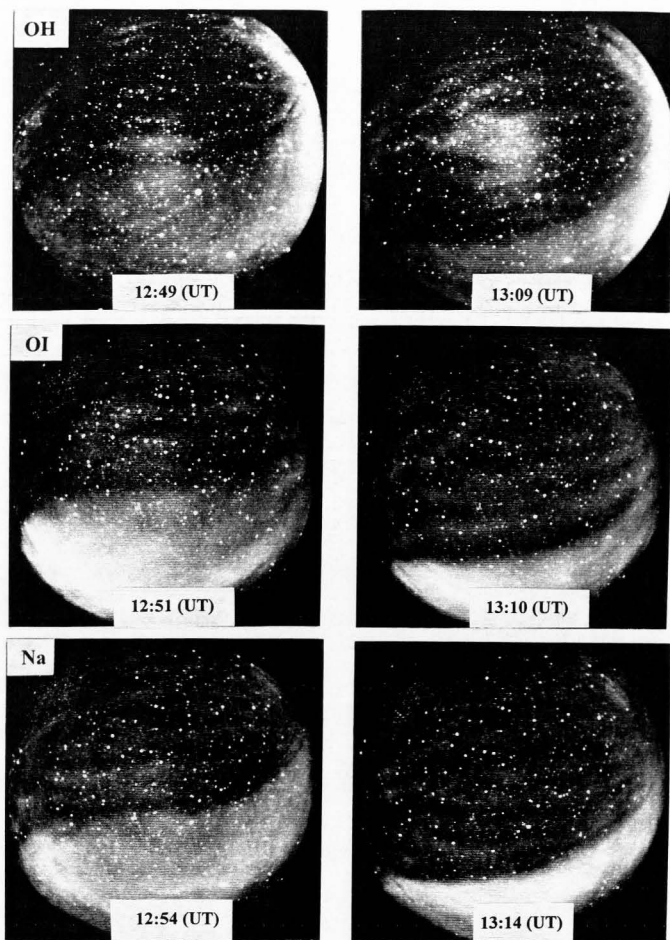


Figure 4.2 Frontal event imaged in the OH, OI, Na emission layers (21 Jan. 1994).

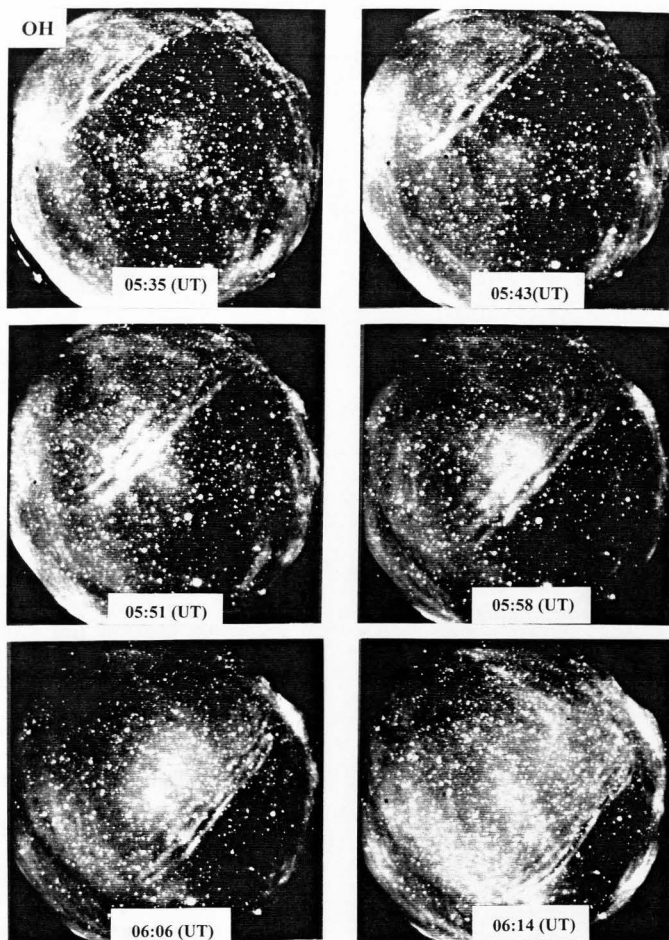


Figure 4.3 A frontal event imaged in the OH emission layer (4 May 1994). This display is similar in appearance to the ALOHA-93 OH data (see Figure 3.1).

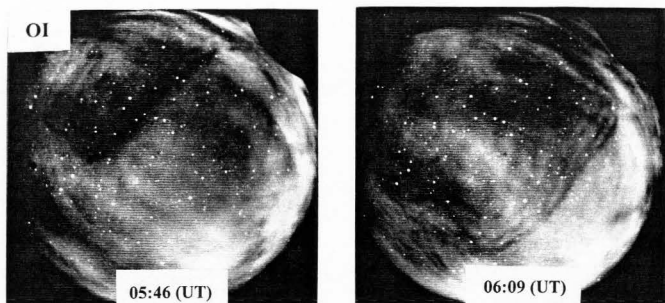


Figure 4.4 The same frontal event as shown in Figure 4.3 but now in the OI (557.7 nm) emission (4 May 1994).

This night was particularly interesting because a second frontal event was observed within 3 hours of the first event. This second event also appeared in the northwestern sky (at $\sim 08:10$ UT) and was again evident in both the NIR OH and OI (557.7 nm) emissions progressive more towards the east at an azimuth of 115° . However, in this case, there was no apparent contrast reversal. The frontal event was also significantly clearer in the OI (557.7 nm) data as compared with the NIR OH image data, which was complicated by presence of another gravity wave pattern around 08:30 UT. This additional wave structure was also evident in the OI (557.7 nm) emission, but less conspicuous (not illustrated here). The average horizontal wavelength of this event was somewhat longer at ~ 17 km, and its average phase speed ($\sim 56 \text{ ms}^{-1}$) was somewhat lower, indicating an observed period of ~ 5.2 min.

4.4.3 10 February 1995

This event was characterized by a sharp change in intensity corresponding to a front, but there were no obvious associated trailing waves. This form of structure is not dealt with by Dewan and Picard's theory, which will be discussed later in Chapter 6. The event was observed to propagate towards the south-southwest ($\sim 204^\circ$) and was most conspicuous in the OI emission. It was first observed at $\sim 10:10$ UT, and it progressed uniformly across the sky at $\sim 38 \text{ ms}^{-1}$ eventually disappearing at $\sim 12:00$ UT in the low elevation southern sky. As this event exhibited no associated wave crests, it is not included in the list of 16 frontal events described in Chapter 5. Two images of this unusual event as detected in the OI emission are given in Figure 4.5.

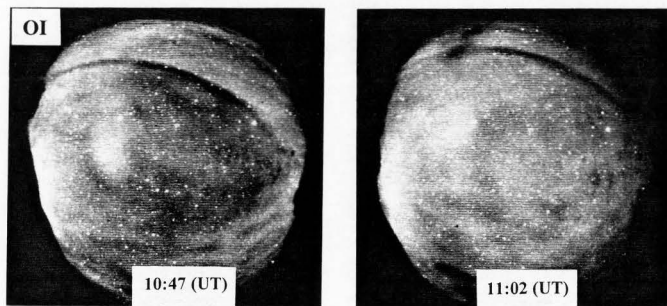


Figure 4.5 A sharp edge with no trailing waves imaged in the OI (557.7 nm) emission (10 Feb. 1995). Dewan and Picard's theory do not deal with this form of structure.

4.4.4 23 January 1996

The wave data evident on this night were quite complex and consisted initially of several separate groups of bands from which emerged a very clear frontal event. Figure 4.6 shows the evolution of this high-contrast event with time in both the OH and OI emissions. The wave front is first seen around 02:40 UT progressing \sim southwards (178°). It is a beautiful event in the OI emission but is also distinct in the OH emission and clearly exhibits a contrast reversal with similar wave parameters to the ALOHA-93 event (average horizontal wavelength and velocity were ~ 26 km and ~ 74 ms⁻¹, respectively, indicating an observed period of ~ 5.5 min). The wave pattern remained coherent and exhibited a limited number of wave crests that appeared to increase in number from 2 to 3 during its passage overhead prior to disappearing into southern sky at $\sim 03:40$ UT.

4.4.5 23 June 1996

This event first appeared in northeastern sky at $\sim 08:30$ UT shortly before dawn. The front was evident in both NIR OH and OI (557.7 nm) emission layers but no contrast reversal was seen. In this case the OH wave pattern was most distinct and consisted of a well defined front with several trailing wave crests. In comparison, the OI front was much less distinct and at times was almost lost in a wealth of similarly oriented, similar horizontal scale-size wave structures that completely filled the camera's field of view. This situation is illustrated in Figure 4.7, which shows coincident OH and OI data over a short ~ 16 -min interval around 10:00 UT. Examination of the OI data alone would

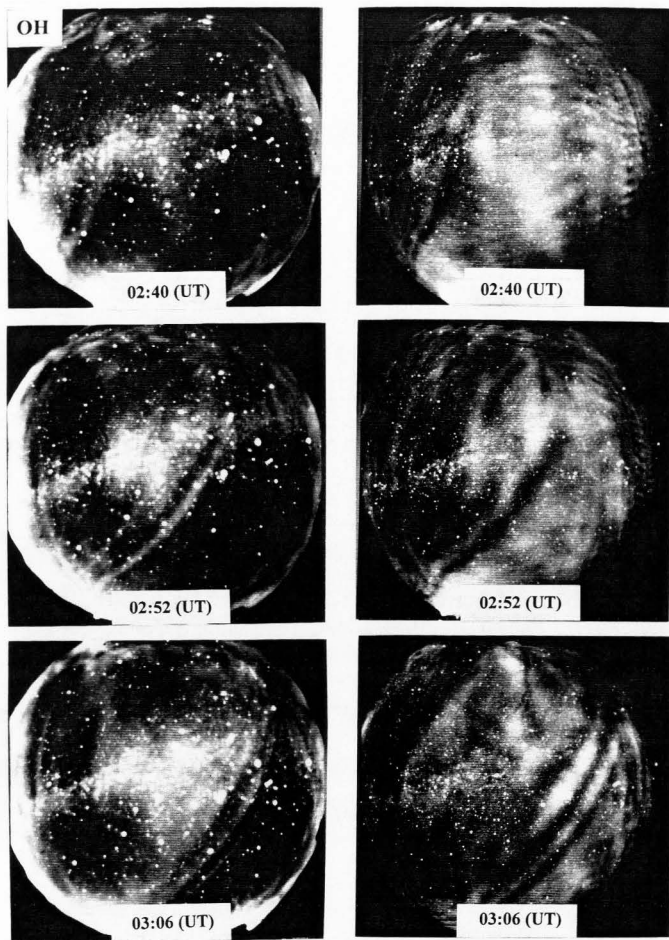


Figure 4.6 A high-contrast frontal event imaged in the OH and OI (557.7 nm) emissions (23 Jan. 1996).

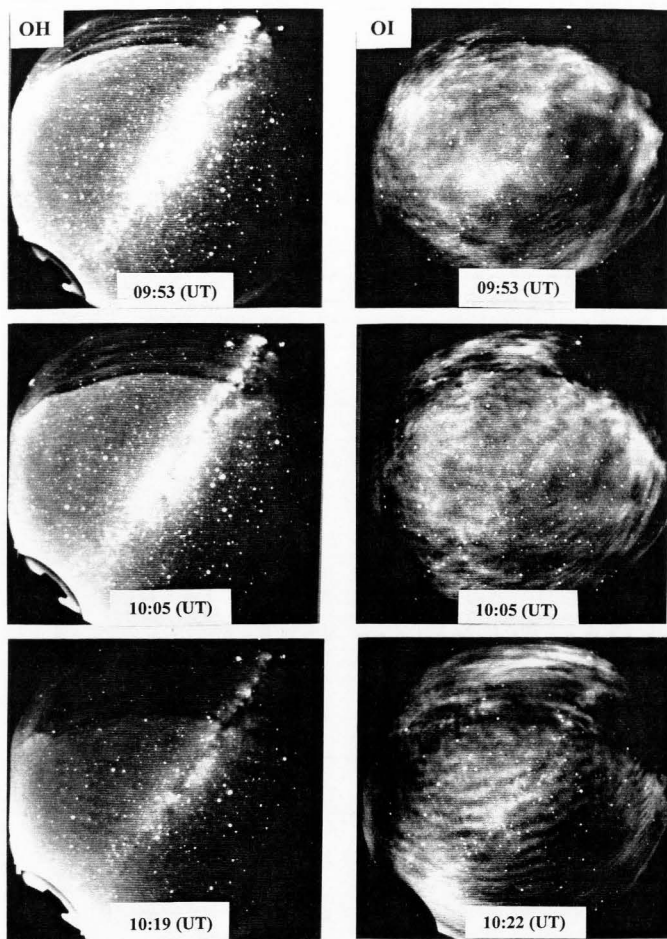


Figure 4.7 Unusual frontal event observed in the OH and OI (557.7 nm) nightglow emissions (23 June 1996).

probably not suggest the passage of a frontal event, yet this is clearly the case in the (lower altitude) OH emission. Note, evidence for very faint structure ahead of the OH wave front is also present in these images. Unfortunately, sunrise (at $\sim 10:30$ UT) limited the measurements before the event could be examined in detail as it passed through the zenith. However, visual inspection of the OH wave pattern reveals that the event was quite dynamic and individual wave crests were observed to "split" to form a shorter wavelength pattern shortly after it was first detected. For this analysis, I chose to measure the shorter period pattern that represented the evolved wave field. The average horizontal wavelength was ~ 14 km, average horizontal phase speed ~ 45 ms^{-1} , yielding an observed period of ~ 5 min and a direction of motion towards the north (azimuth $\sim 7^\circ$).

4.4.6 6 July 1997

On this night two frontal events were observed simultaneously in both the NIR OH and the OI (557.7 nm) emissions. One event propagated into the northeastern sky ($\sim 45^\circ$) while the other traveled in a more northerly direction ($\sim 13^\circ$). Both events were first detected at about 9:30 UT and appeared to exhibit an OH/OI contrast reversal. The frontal event that progressed into the northern sky was much clearer in the OH emission than in the OI emission. (Indeed, no measurements of the OI event were possible due to strong interference with the northeastern wave pattern.) The geometry of these two frontal events, as detected near simultaneously in the OH and OI emission, is shown in Figure 4.8. The average horizontal wavelength of the northeastern wave was ~ 18 km and its horizontal phase speed ~ 32 ms^{-1} , giving a relatively long observed period of

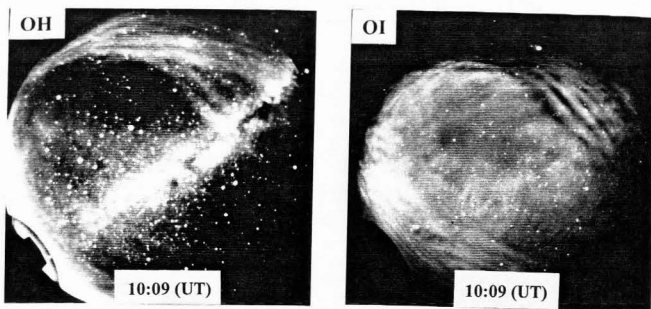


Figure 4.8 Dual frontal events imaged in the OH and OI (557.7 nm) nightglow emissions (6 July 1997).

~9.6 min. The northerly wave pattern exhibited a significantly longer horizontal wavelength of ~22 km but a similar phase speed, indicating an observed period ~11.6 min. Full details of these and the other frontal events studied are given in Table 5.1 of Chapter 5.

4.5 Bear Lake Frontal Event Occurrence Frequency

I have examined 29 months of data from the period from 1994 to 1997. Specifically this covers the period January ~ June 1994, January ~ October 1995, January ~ October 1996, June ~ August 1997. It seems that fronts are not common features because they did not appear even once a month on average. However, from the data set obtained so far, there are significantly more frontal events during summer months (May ~ September) than at any other time of year. A second “peak” also is evident in January. However, we cannot say here that frontal events are predominantly seen in the summer as

our data are sparse, particularly for November and December. Table 4.1 shows the Bear Lake frontal event occurrence frequency on a monthly basis.

Visual examination of the CCD data has yielded 16 events that can be classified as frontal-like events. All of these events were characterized by a well-defined sharp leading edge and most exhibited several trailing waves. However, the step-like change in intensity induced by the passage of the front was not always evident in both OH and OI

Table 4.1 Bear Lake Frontal Event Monthly Occurrence

Month	94	95	96	97	Total
January	1	0	1	X	2
February	1	1	0	X	2
March	0	0	0	X	0
April	0	0	0	X	0
May	2	3	0	X	5
June	0	0	1	X	1
July	X	0	0	3	3
August	X	1	0	0	1
September	X	2	0	X	2
October	X	0	0	X	0
November	X	X	X	X	0
December	X	X	X	X	0
Total	4	7	2	3	16

emissions. In fact, only 8 of the 16 events were evident in both emissions. Moreover, only half of the eight events where the waves were clearly evident in both emissions exhibited a reversal in contrast. As will be shown later, contrast reversal is not a requirement for a frontal event. A summary of the derived wave parameters for these events is given in the following chapter.

CHAPTER 5

RESULTS

5.1 Determination of Wave Characteristics

As a result of analyzing 16 Bear Lake frontal events, the average horizontal wavelength of the trailing waves was found to be ~15 to 18 km, the average horizontal phase speed was ~47 ms⁻¹, and hence the average observed period was ~6 min. Table 5.1 summarizes the individual wave parameters determined from this analysis, which covers the period January '94 to July '97.

Table 5.1 Summary of Derived Wave Parameters for 16 Frontal Events Imaged at Bear Lake Observatory, Utah (*represents event discussed in Chapter 4).

Event	UT Date	UT Time	Nightglow Emission	λ_x (km)	v_x (ms ⁻¹)	τ_{ob} (min)	Azimuth ($\pm 5^\circ N$)
*1	21 Jan. 1994	12:39 ~	OH	22.1 \pm 1.5	52 \pm 1	7.2	183
		12:45 ~	Na	19.3 \pm 1.5	56 \pm 2	5.7	184
		13:04 ~	OI	23.7 \pm 0.7	57 \pm 1	6.9	185
		13:06 ~					
		13:16					
2	16 Feb. 1994	09:18 ~	OI	6.2 \pm 0.3	15 \pm 1	7.1	180
		09:27					
*3	4 May 1994	05:43 ~	OH	10.4 \pm 0.1	60 \pm 1	2.9	129
		05:51 ~	OI	12.1 \pm 0.3	75 \pm 2	2.7	130
		06:01					
4	4 May 1994	08:35 ~	OH	17.5 \pm 0.8	55 \pm 2	5.3	116
		08:42 ~					
		08:27 ~	OI	17.1 \pm 0.7	57 \pm 4	5.0	114
		08:34					
5	4 Feb. 1995	07:17 ~	OI	11.7 \pm 1.1	51 \pm 2	3.9	352
		07:32					

Table 5.1 Continued

Event	UT Date	UT Time	Nightglow Emission	λ_x (km)	v_x (ms ⁻¹)	τ_{ob} (min)	Azimuth ($\pm 5^\circ$ N)
6	4 May 1995	04:53 ~	OH	15.1 \pm 0.4	46 \pm 1	5.5	102
		05:10					
		04:55 ~	Na	----	45 \pm 1	---	102
		05:13					
7	30 May 1995	05:01 ~	OI	15.2 \pm 0.7	43 \pm 1	5.9	100
		05:10					
8	30 May 1995	05:33 ~	OI	13.3 \pm 0.2	29 \pm 1	7.7	51
		05:38					
9	26 Aug. 1995	05:42 ~	OI	9.9 \pm 0.3	29 \pm 2	5.7	44
		05:51					
10	1 Sep. 1995	08:15 ~	OI	16.4 \pm 0.6	69 \pm 2	3.9	358
		08:23					
11	1 Sep. 1995	06:21 ~	OH	22.2 \pm 0.0	41 \pm 2	9.0	358
		06:25					
		06:21 ~	OI	18.4 \pm 0.4	51 \pm 1	6.0	6
12	23 Jan. 1996	06:30					
		06:21 ~	OI	15.4 \pm 0.4	60 \pm 1	4.3	323
*12	23 Jan. 1996	12:49 ~	OH	25.8 \pm 0.2	72 \pm 3	5.3	178
		12:57					
		02:57 ~	OI	25.6 \pm 0.3	77 \pm 5	5.6	177
*13	23 Jun. 1996	03:06					
		10:19 ~	OH	12.4 \pm 0.5	42 \pm 1	4.9	7
		10:28					
14	1 Jul. 1997	10:22 ~	OI	14.5 \pm 0.1	48 \pm 1	5.0	5
		10:31					
		08:21 ~	OH	15.5 \pm 0.6	42 \pm 2	6.2	25
*15	6 Jul. 1997	08:27					
		08:14 ~	OI	16.2 \pm 0.2	41 \pm 1	6.6	29
		08:26					
16	6 Jul. 1997	10:03 ~	OH	18.1 \pm 0.3	32 \pm 2	9.4	46
		10:09					
		09:57 ~	OI	18.4 \pm 1.3	32 \pm 1	9.7	40
Average Value		10:09					
		09:55 ~	OH	22.3 \pm 0.8	32 \pm 1	11.6	13
		10:01					
		Average Value	OH	18.1	47	6.7	
			OI	14.6	46	5.4	

5.2 Intensity Measurements of Frontal Events

From the nightglow intensity measurements of frontal events, we have determined that they are all characterized by a sudden change in intensity at the front, but not all events show a contrast reversal between the OH (~87 km) and OI (~96 km) emission structures. To investigate the relative intensity perturbations induced by the passage of the front and the associated wave motions, it is necessary to flat-field the data to remove the effects of lens vignetting and line-of-sight enhancements due to the all-sky viewing geometry. A simple method of flat-fielding the data is to average together several images (typically ten) to determine the instrumental and sky flat-field response. This averaged image is then subtracted from the data image to remove the unwanted optical distortions. The resultant image data then contain information that can be compared in intensity at any part of the image. A full description of this method for quantitative intensity measurements is given in *Garcia et al.* [1997]. The following data were all flat-fielded before the intensity and contrast measurements were made.

Table 5.2 shows measurements of contrast ratios for the fronts and associated trailing waves for each of the 16 frontal events observed. The contrast ratio is defined by the relation $(I_{\max} - I_{\min}) \times 100\% / I_{\max}$ where I_{\max} is a measure of the peak brightness and I_{\min} an adjacent brightness minimum. For the fronts, this measurement represents the "step-like" change in intensity that characterizes this type of event. The average contrast ratios for the OH and OI fronts were found to be ~11% and ~8%, respectively. The average contrasts of the trailing OH and OI waves were ~6% and ~5%, respectively.

Table 5.2 Contrast Measurements of the Front and Trailing Waves of the 16 Frontal Events. (X : no event, --- : no clear front, * : data discussed in Chapter 4)

Event	Date	Time (UT)	Coordinates (x_1, y_1), (x_2, y_2)	OH Contrast (%)		OI Contrast (%)	
				Front	Wave	Front	Wave
*1	21 Jan. 1994	13:05	(187,86), (241,490)	9.3	5.3	7.9	3.5
2	16 Feb. 1994	09:27	(124,151), (136,250)	x	x	4.8	2.9
*3	4 May 1994	05:50	(172,191), (315,343)	10	7.9	8.5	4.3
4	4 May 1994	08:34	(56,163), (131,210)	10	2.9	6.2	2.8
5	4 Feb. 1995	07:17	(106,253), (121,415)	x	x	3.6	2.5
6	4 May 1995	05:10	(349,184), (113,146)	7.0	4.5	---	5.0
7	30 May 1995	05:33	(99,232), (0,035)	x	x	10	7.3
8	30 May 1995	05:51	(394,103), (281,240)	x	x	6.9	4.5
9	26 Aug. 1995	08:19	(398,400), (204,240)	x	x	13	4.2
10	1 Sep. 1995	06:21	(421,257), (254,114)	---	5.5	11	7.8
11	1 Sep. 1995	06:21	(438,367), (346,348)	x	x	9.6	4.0
*12	23 Jan. 1996	02:57	(216,250), (381,375)	13	4.8	12	7.2
*13	23 Jun. 1996	10:22	(224,30), (210,295)	16	6.9	6.8	3.3
14	1 Jul. 1997	08:26	(360,181), (243,327)	7.7	2.9	4.2	2.5
*15	6 Jul. 1997	10:03	(396,143), (245,259)	---	9.3	---	15
16	6 Jul. 1997	09:57	(233,20), (219,245)	13	5.6	x	x
Average Contrast Ratio				10.8	5.6	8.0	5.1

Both of these averages are somewhat smaller than those determined from the Hawaiian data reported by *Taylor et al.* [1995c]. Examination of Table 5.2 reveals a considerable spread in the contrast values, particularly for the frontal ratios. The range of contrast for the front was ~7-16% for the OH data and ~4-12% for the corresponding OI data. These are significantly lower than the *Taylor et al.* [1995c] observations, which found contrasts of ~33% for the OH data and ~24% for the OI data, highlighting the remarkable nature of that event. Contrast measurements of the trailing waves varied from ~3-7% for both emissions with one exception--an unusually large amplitude wave observed on 6 July 1997 (event 15), which indicated a contrast of ~15% for the OI data, which compares with that of the Hawaiian observations (see Chapter 3). In general, the contrast ratios associated with fronts are significantly larger than the perturbations induced by the more frequently imaged bands that typically exhibited contrast of 5 to 10%.

Figures 5.1 to 5.6 show intensity profiles measured from the OH and/or OI wave data structure associated with the six frontal events described in Chapter 4. In each case the intensity scan was made normal to the front and in the same direction as its motion. Thus, the left side of each scan starts behind the front and the right side stops ahead of the front. Figure 5.2 and Figure 5.6 show a clear contrast reversal between the OH and OI emission structures, whereas in Figure 5.5 no contrast reversal is seen. Figure 5.6 is interesting as it shows no clear front at all, implying that the difference in intensity between the front and trailing waves was small on this occasion.

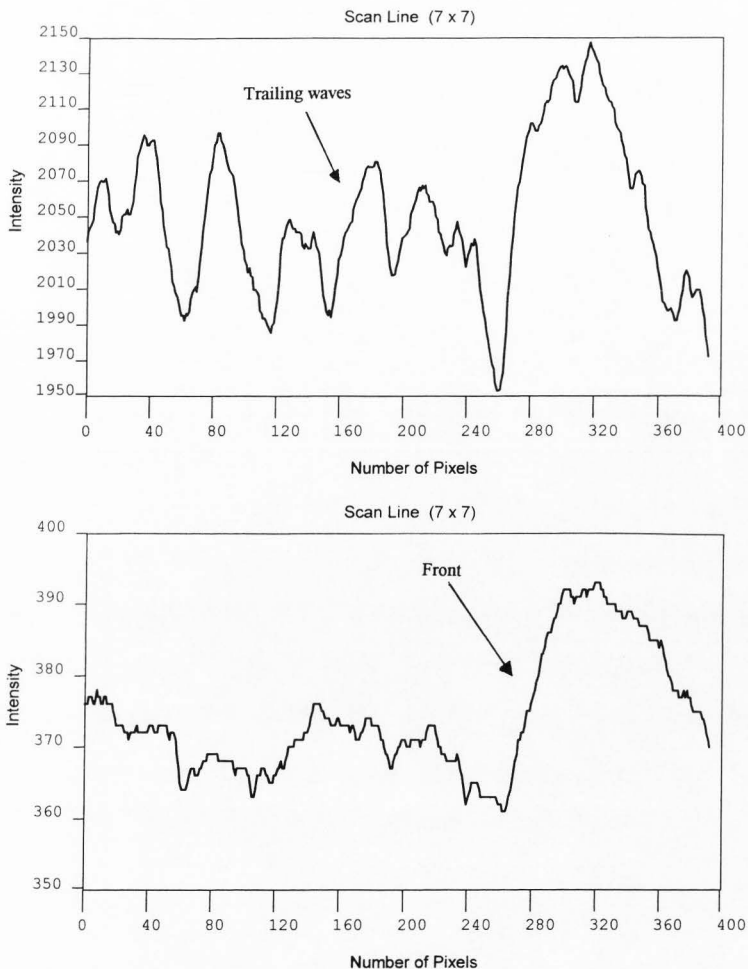


Figure 5.1 Intensity profiles of OH (top) and OI (bottom) emission at 13:05 UT 21 Jan. 1994, BLO (event 1). No obvious contrast reversal is evident. The front is located between position 260 to 300 pixels. Note the clear oscillation in the OH trailing waves.

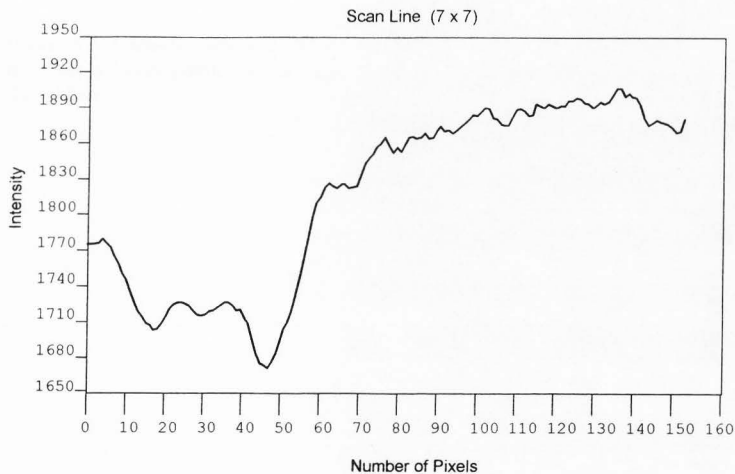
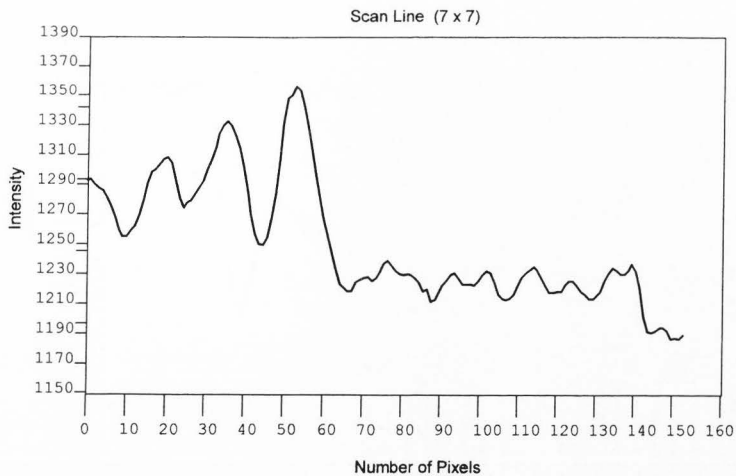


Figure 5.2 Intensity profiles of OH (top) and OI (bottom) emission at 05:50 UT 4 May 1994, BLO (event 3). The front lies between position 50 to 65 pixels and is very conspicuous. Note the clear contrast reversal between the OH and OI data.

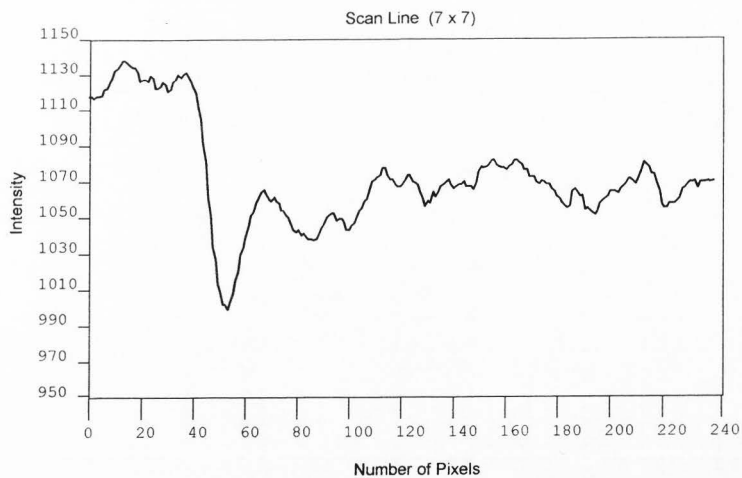


Figure 5.3 Intensity profiles of OI emission at 11:02 UT 10 Feb. 1995, BLO. The OI front lies between position 40 to 50 pixels. (The OH front was very faint and is not shown here).

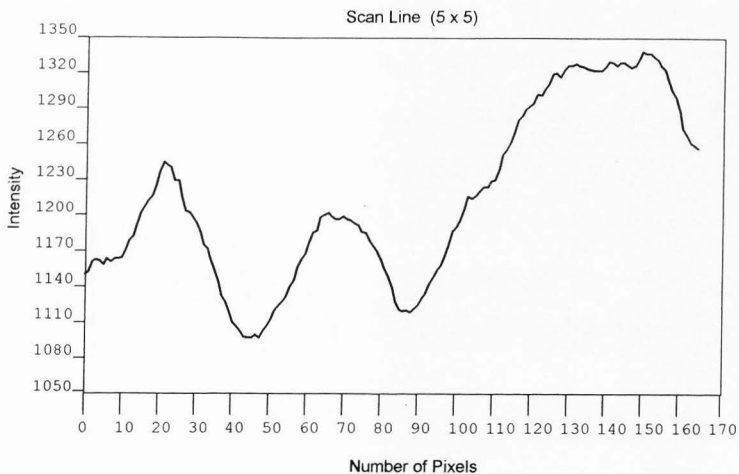
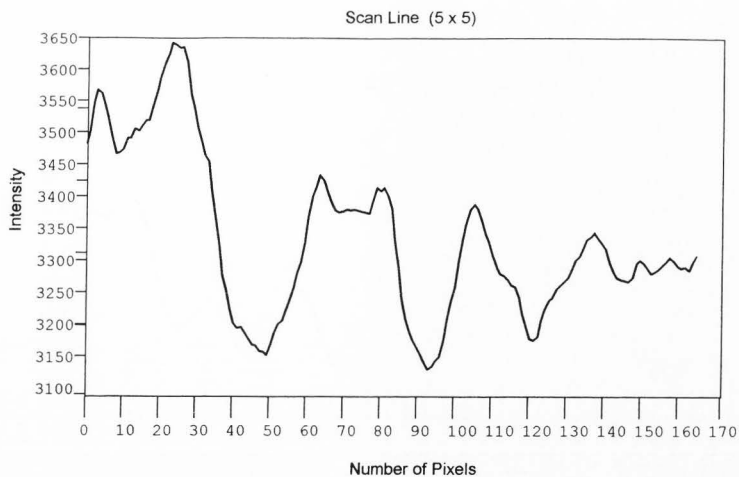


Figure 5.4 Intensity profiles of OH (top) and OI (bottom) emission at 02:57 UT 23 Jan. 1996, BLO (event 12). No contrast reversal. The front is between 25 to 50 pixels in the OH but appears to be between 100 - 130 in the OI data. The trailing waves in both cases are of very well defined.

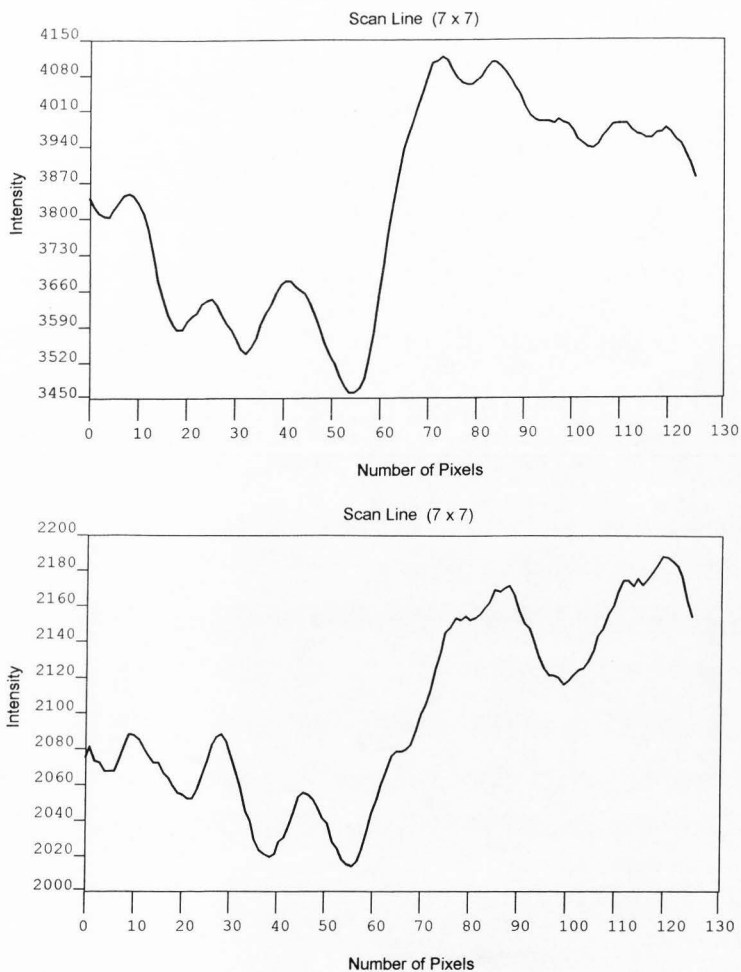


Figure 5.5 Intensity profiles of OH (top) and OI (bottom) emission at 10:22 UT 23 June 1996, BLO (event 13). This is an excellent example of a clear front in both emissions with no contrast reversal. The front lies between position 55 to 80 pixels.

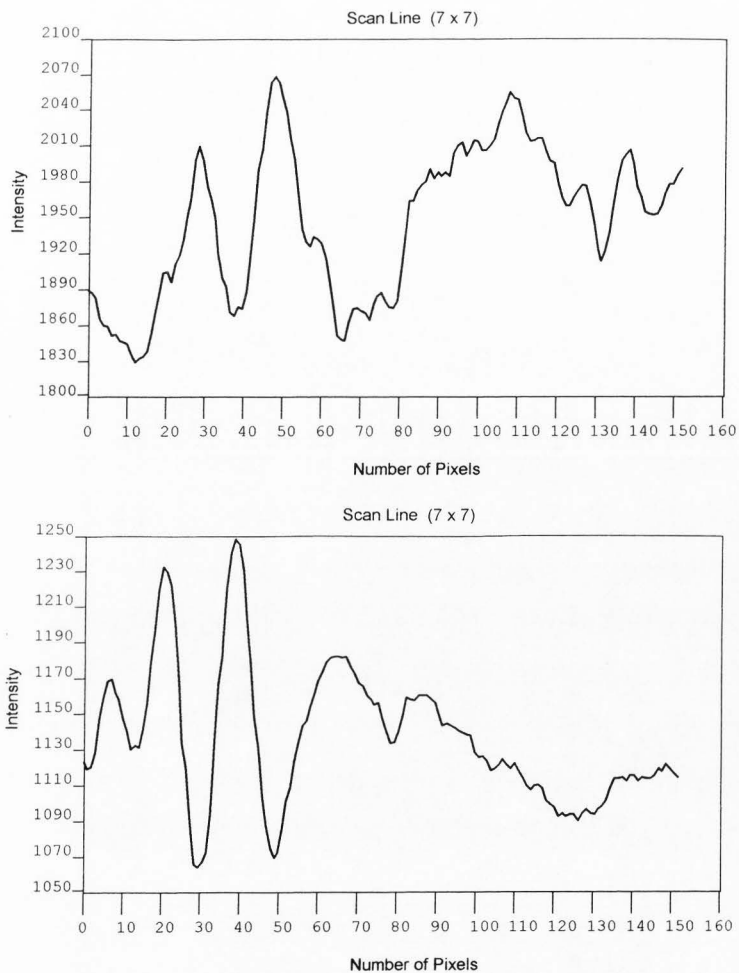


Figure 5.6 Intensity profiles of OH (top) and OI (bottom) emission at 10:03 UT 6 July 1997, BLO (event 15). The front lies between position 40 to 50 pixels and is not clear at all in these plots but is quiet evident in the image data Figure 4.4.6.

CHAPTER 6

DISCUSSION

6.1 Mesospheric Bores

Dewan and Picard [1998] have attempted to describe the frontal events reported by *Taylor et al.* [1995e] in terms of an internal mesospheric “undular bore” in their paper entitled “On Mesospheric Bores.” They draw heavily on the observed wave parameters reported by Taylor and colleagues and have developed a simple model that is based on the theory of bores in river channels, which bear a remarkable resemblance to the mesospheric frontal events reported here.

Figure 6.1 shows an undular tidal bore on the River Mersey, England. Tidal bores travel up river and are due to funneling of water into narrowing channel resulting in a step-like change in the water level at the leading edge. In an analogous manner the mesospheric bore theory is based on the assumption that as the wave front passes through the atmosphere it causes an abrupt raising or lowering of the various airglow layers (OH, OI, Na, and O₂). This theory is founded on the fact that a significant change in the OH rotational temperature (~20 K) was observed during the passage of the Hawaiian frontal event (see Chapter 3). According to *Makhlouf et al.* [1990], such a temperature increase can be associated with an altitude decrease (due to adiabatic compression) of ~2 km in this case. However, the theory fails to account for the apparent delay in the sudden change in airglow brightness relative to the observed change in temperature reported by *Taylor et al.* [1995c].

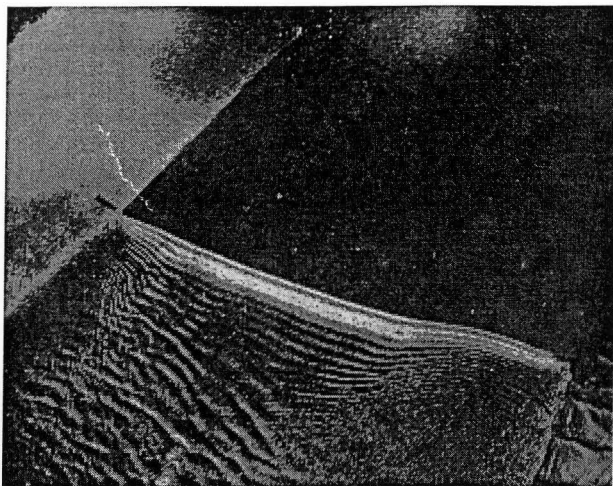


Figure 6.1 Undular tidal bore on the River Mersey, England [Tricker,1965]. Note the clear similarity in event morphology to the mesospheric data of Chapter 4.

Assuming that frontal events are the manifestation of mesospheric undular bores at airglow altitudes, then the contrast reversal that is sometimes observed between the lower and the higher altitude image data would be explained if we assume that: (1) the bore existed in a horizontal wave guide or channel at ~90-94 km (in the case of the Hawaiian data), and (2) acted to depress the OH and Na layers downwards, thereby increasing the brightness of these emissions and at the same time elevate the O₂ and OI layers upwards, which would cause these emissions to reduce in brightness. In the case of a river bore, the channel has a rigid bottom. In the case of the atmosphere, a channel could exist in a form of a duct. To quote Dewan and Picard, this duct would exist as “a

layer of air bounded by a neutrally stable atmosphere" (assuming a windless condition) according to *Mahapatra et al.* [1991, p. 1468]. Figure 6.2 shows a simplified model for a bore of height $h_1 - h_0$ propagating through undisturbed water of depth h_0 .

It is well known that the thermocline, an upper region of strong stability in an oceanic bore, can support internal waves. The atmospheric bore is assumed to exist in a region of high stability bounded by regions of low or neutral stability above and below it. According to *Lighthill* [1978], there are two kinds of modes in oscillation of the thermocline called "sinuous" and "varicose." In the first case, the top and the bottom of the thermocline move together in phase. In the latter case, they oscillate 180° out of phase. A mid-plane about which the waves oscillate symmetrically behind the bore plays the same role of the rigid bottom of the water channel. Figure 6.3 shows a symmetrical undular bore with symmetry plane S where the displacement is zero in analogy with the rigid bottom in channel bores. According to lidar observations by *Dao et al.* [1995]

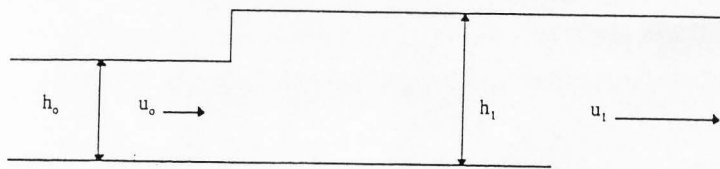


Figure 6.2 Schematic diagram showing a model of a bore of height $h_1 - h_0$ propagating to undisturbed water of depth h_0 . The frame of reference of this figure is where the bore is stationary. In the frame where the bore moves into still water, u_0 would be the bore's velocity and u_1 is the velocity of the water at the rear of the bore front [*Dewan and Picard*, 1998].

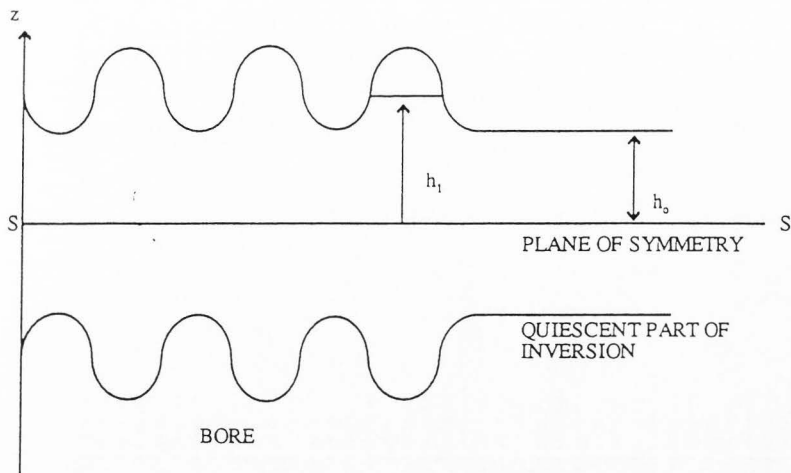


Figure 6.3 Schematic diagram showing a symmetrical undular bore with symmetry plane *S* [Dewan and Picard, 1998]. In this case it is easy to see the OI and OH waves could exhibit contrast reversal.

obtained during the ALOHA-93 campaign (but not on the night of the frontal event), the existence of such a channel, which is characterized by a region of increased stability in the atmosphere, can be caused by a sudden temperature increase near 90 km. Most recently, Huang *et al.* [1998] explained the observations of the localized temperature increase reported by Dao *et al.* [1995] as being due to a gravity-wave critical-layer interaction in which case deposition of momentum due to the critical layer would accelerate the mean flow to an instability condition resulting in turbulence and subsequent heating.

As already mentioned, the reversal in contrast (180° out of phase) of the wave pattern for the two lower airglow layers (OH and Na) compared with the two upper

layers (O_2 and OI) reported in the Hawaiian data indicates that on this occasion the bore might have been fortuitously centered between the Na (~ 90 km) and O_2 (~ 94 km) airglow regions. If this were the case, then the observation of no contrast reversal, as shown in Figure 5.5, could easily be explained by the bore residing either below or above all four emission layers. Although tides in the ocean are the source of river bores, it is not clear that atmospheric tides are a possible source of mesospheric bores.

6.2 Comparison with Bore Theory

The theory of mesospheric undular bores derived by *Dewan and Picard* [1998] can be applied immediately to several aspects of our data. First, the existence of undular bores in the MLT region would by analogy with the river bores explain their observed morphology. In all but one frontal event, a limited number of trailing wave crests were observed in keeping with the concept of an undulating bore. Furthermore, the number of wave crests appeared to increase with time for several of these events. This aspect of the observations is predicted by Dewan and Picard's theory at a rate of approximately three crests per hour. It is difficult to compare this rate with our data, which were often limited in duration by the observing conditions. However, we can say that an increase of three crests per hour would be an upper limit based on the available data. The bore theory explains the existence of the front as a trapped or ducted wave motion and as such predicts a relatively high phase speed and a short observed period of ~ 5 min (assuming a zero wind condition). This prediction is most consistent with our observations and those of Taylor et al., which show phase speeds of up to 76 ms^{-1} and observed periods as low as 2.7 min (i.e., below the Brunt period), indicating possible wind effects on the observed

wave periods. However, some frontal events exhibited significantly lower phase speed (as low as 30 ms^{-1}) and consequently observed periods as high as 12 min. Dewan (private communication) has indicated these events also fall into the range of phase speeds and periods that could be expected for ducted waves depending on the background MLT conditions.

Of considerable importance is the (now simple) explanation for the observed contrast reversal between the OH and OI emission structure that we have shown in this analysis is apparent for some, but certainly not all frontal events. The explanation proposed by Dewan and Picard relates this phenomenon to the relative location in altitude of the bore with respect to the airglow emission layers. In summary, this study has revealed several events that are qualitatively similar to the original observations of Taylor et al. The results show that such events are not unique but they are certainly not common (compared with other gravity wave structure described by bands and ripples). The close proximity of the airglow layers to the mesopause (atmospheric temperature minimum, see Figure 1.1) may play a role in the existence of thermal ducts capable of trapping the wave motions. Alternatively, Doppler ducts at MLT heights (due to regions of different wind shear) are also capable of trapping short-period waves [Isler et al., 1998]. The exact location of the duct is not known for any of our data, but observations of no contrast reversal indicate that it would be located either above or below both of the OH and OI emission layers. A cornerstone of the bore theory is the observation of a temperature change (increase) observed as the front passed overhead at Hawaii during the ALOHA-93 campaign, which in turn suggested a displacement of $\sim 2 \text{ km}$ induced by

the passage of the bore. Unfortunately, no temperature data are available for comparison with our BLO data set to confirm this finding.

CHAPTER 7

CONCLUSIONS AND RECOMMENDATIONS

FOR FUTURE STUDIES

Gravity waves play a very important role in the dynamics of MLT region because they can transfer large amounts of energy and momentum from the troposphere into the upper atmosphere [*Fritts and Vincent, 1987*]. Frontal events have been called "spectacular gravity wave events" because they have very distinguishable characteristics that set them apart from other, more frequently observed, internal gravity waves. Furthermore, they are conspicuous by their relatively high contrast and their ability to cause reversals in contrast for the differing airglow emissions residing at different altitudes.

Theoretical research on mesospheric frontal events is quite recent and is based on their observed properties in the troposphere (morning glories), oceans, and some rivers, all of which are well documented phenomena. Several models exist to explain oceanic and tropospheric bores, but only the undular bore model has so far been invoked to explain the (then) isolated observations by Taylor et al. of a single mesospheric frontal event. This model provides several ways to test its validity. The BLO data set agrees well in principle with this model, but there is a clear need for more comprehensive measurements of mesospheric winds and the associated temperature changes during the passage of such events. These measurements could be made at BLO or some other suitable site and are necessary to isolate and characterize the nature of the ducted wave motion.

The most prominent characteristic of a frontal event is its sharp leading edge, followed by a limited number of trailing waves. Contrast reversal between the OH (~87 km) and OI (~96 km) emissions is characteristic but not an essential feature. In this thesis I have shown cases of no contrast reversal and in one instance no associated waves, yet the front was very prominent (see Figure 4.4). The reversal in contrast is assumed to be the response to an adiabatic temperature change as a result of a vertical displacement of the airglow layers by a disturbance propagating in a horizontal wave guide. Such disturbances do not appear to be common and major unanswered questions are, therefore, what events give rise to bore-like motions in the atmosphere? How often do they occur, and how far can they propagate horizontally before they dissipate?

The measurement of the frontal events of Bear Lake Observatory, Utah (41.9°N) from 1994 to 1997 using a new, high-sensitivity CCD camera indicates a typical horizontal wavelength of 15 to 25 km, a mean horizontal phase speed of ~50 ms⁻¹, and an average period of 3 to 12 min. According to *Taylor et al.* [1995e], the average horizontal wavelength of the frontal event observed over Hawaii (21°N) was 19.3 ± 0.7 km, the average horizontal velocity was about 76 ms⁻¹, and the average period was 4.2 ± 0.2 min. The mid-latitude BLO data, therefore, exhibit properties that encompass these measurements. Furthermore, to date most observations of frontal events were made in the summer months and more observations are necessary at other times of the year to confirm these findings.

Imaging techniques have been developed considerably over the past 25 years for investigating of night sky phenomena. The most recent and powerful instrument is an all-

sky (180°) CCD camera used in this experiment. But still more advanced imaging techniques such as two-dimensional mesospheric temperature mapping are necessary to investigate gravity wave signatures in more detail. With the availability of new data, developments in the bore models will surely ensue.

Generally, the sources of most small-scale internal gravity waves are considered to be thunderstorms, fronts, jet streams, or orographic force over mountainous areas, which are thought to generate quasi-monochromatic waves (as evidenced in bands). On the other hand, mesospheric bores exhibit quite dissimilar characteristics in their morphology and in their relatively high contrast. In this thesis I have not investigated the sources of the observed frontal events discussed herein. Source studies are inherently difficult, involving ray tracing or other techniques to isolate the disturbances, and as such are quite rare [e.g., *Taylor and Hapgood*, 1988]. However, this type of research is both promising and necessary. If the sources prove to be of the same type as those responsible for the more common wave structures, then we should also investigate what causes the difference between frontal events and band-type gravity waves. In summary, this study suggests that within the current limits of the available data, the bore model proposed by Dewan and Picard adequately explains the most prominent properties of frontal events so far recorded at BLO.

REFERENCES

- Armstrong, E. B., Irregularities in the 80-100 km region: A photographic approach, *Radio Sci.*, 21(3), 313, 1986.
- Barbier, D., and J. Glaume, Correlations entre les intensités de diverses radiations de la luminescence atmosphérique nocturne, *Ann. Geophys.*, 16, 56, 1960.
- Baker, D. J., and A. T. Stair Jr., Rocket measurements of the altitude distributions of the hydroxyl airglow, *Phys. Scr.*, 37, 611, 1988.
- Barth, C. A., and A. F. Hildebrandt, the 5577 Å airglow emission mechanism, *J. Geophys. Res.*, 66, 985, 1961.
- Bates D. R., and M. Nicolet, The theory of the emission spectrum of the OH molecule in the night sky spectrum, (translated title), *Compt. Rend.*, 230, 1943, 1950.
- Carter, D. A., and B. B. Balsley, The summer wind field between 80 and 93 km observed by the MST radar at Poker Flat, Alaska (65°N), *J. Atmos. Sci.*, 39, 2905-2915, 1982.
- Chanin, M. L., and A. Hauchecorne, Lidar observation of gravity and tidal waves in the stratosphere and mesosphere, *J. Geophys. Res.*, 86, 9715-9721, 1981.
- Chanin, M. L., Observation of the propagation and dispersion of gravity waves in the middle atmosphere, paper presented at Sixth International Symposium on Solar-Terrestrial Physics, SCOSTEP, Toulouse, France, 1986.
- Chapman, S., Some phenomena of the upper atmosphere, (Bakerian lecture), *Proc. Roy. Soc.*, A131, 353, 1931.
- Chapman, S., Notes on atmospheric sodium, *Astrophys. J.*, 90, 309, 1939.
- Clairemidi, J., M. Herse, and G. Moreels, Bi-dimensional observations of waves near the mesopause at auroral latitudes, *Planet. Space Sci.*, 33(9), 1013, 1985.
- Crawford, J., P. Rothwell, and N. Wells, Simulating experiments for Spacelab, *Nature*, 257, 650, 1975.
- Dao, P. D., R. Farley, X. Tao, and C. Gardner, Linear observations of the temperature profile between 25 and 103 km: Evidence of a strong tidal perturbation, *Geophys. Res. Lett.*, 22, 2825-2828, 1995.

- Dewan, E. M., and R. H. Picard, On mesospheric bores, *J. Geophys. Res.*, 103(D6), 6295-6305, 1998.
- Elvey, C. T., Note on the spectrum of the airglow in the red region, *Astrophys. J.*, 111, 432, 1950.
- Frezal, M. E., M. Glass, J. L. Fellous, and M. Massebeuf, Simultaneous meteor radar observations at Monpazier (France 44°N) and Punta Borinquen (Puerto Rico, 18°N), III, The latitudinal variations of the energy of gravity waves (2-8 h) in the high mesosphere, *J. Atmos. Terr. Phys.*, 43, 543-547, 1981.
- Fritts, D. C., J. R. Isler, and G. E. Thomas, Wave breaking signatures in noctilucent clouds, *Geophys. Res. Lett.*, 20, 2039, 1993.
- Fritts, D. C., and P. K. Rastogi, Convective and dynamical instabilities due to gravity wave motions in the lower and middle atmosphere: Theory and observations, *Radio Sci.*, 20, 1247-1277, 1985.
- Fritts, D. C., and R. A. Vincent, Mesospheric momentum flux studies at Adelaide, Australia: Observations and gravity wave-tidal interaction model, *J. Atmos. Sci.*, 44, 605, 1987.
- Garcia, F. J., M. J. Taylor, and M. C. Kelly, Two-dimensional spectral analysis of mesospheric airglow image data, *Appl. Opt.*, 36(29), 1997.
- Gardner, C. S., Introduction to ALOHA / ANLC-93: The 1993 airborne lidar and observations of the Hawaiian airglow/airborne noctilucent cloud campaigns, *Geophys. Res. Lett.*, 22, 2789, 1995.
- Gardner, C. S., and D. G. Voelz, Lidar studies of the nighttime sodium layer over Urbana, Illinois, 2, Gravity waves, *J. Geophys. Res.*, 92, 4673, 1987.
- Greer, R. G. H., and G. T. Best, A rocket-borne photometric investigation of the oxygen lines at 5577 Å and 6300 Å, the sodium D-lines and continuum at 5300 Å in the night airglow, *Planet Space Sci.*, 15, 1857, 1967.
- Hapgood, M. A., and M. J. Taylor, Analysis of airglow image data, *Ann. Geophys.*, 38(6), 805, 1982.
- Hargreaves, J. K., *The Upper Atmosphere and Solar-Terrestrial Relations—An Introduction to the Aerospace Environment*, Van Nostrand Reinhold, Wokingham, Berkshire, UK, 1979.

- Haurwitz, B., and B. Fogle, Wave forms in noctilucent clouds, *Deep-Sea Res.*, 16, 85, 1969.
- Hecht, J. H., R. L. Walterscheid, D. C. Fritts, J. R. Isler, D. C. Senft, C. S. Gardner, and S. J. Franke, Wave breaking signatures in OH airglow and sodium densities and temperatures, 1, Airglowimaging, Na lidar, and MF radar observations, *J. Geophys. Res.*, 102(D6), 6655, 1997.
- Hecht, J. H., R. L. Walterscheid, and M. N. Ross, First measurements of the two-dimensional horizontal wave number spectrum from CCD images of the nightglow, *J. Geophys. Res.*, 99, 11449, 1994.
- Hines, C. O., Internal atmospheric gravity waves at ionospheric heights, *Can. J. Phys.*, 38, 1441-1481, 1960.
- Hines, C. O., On the nature of traveling ionospheric disturbances launched by low-altitude nuclear explosions, *J. Geophys. Res.*, 72, 1877-1882, 1967.
- Hines, C. O., A possible source of waves in noctilucent clouds, *J. Atmos. Sci.*, 25, 937, 1968.
- Hirota, I., and T. Niki, A statistical study of inertia-gravity waves in the middle atmosphere, *J. Met. Soc. Japan*, 63, 1055-1066, 1985.
- Houghton, J. T., *The physics of atmospheres*, second edition, Cambridge University Press, Cambridge, UK, 1989.
- Huang, T. Y., T.-F. Tuan, X. Li, E. M. Dewan, and R. H. Picard, Sudden narrow temperature inversion-layer formation in ALOHA-93 as a critical-layer-interaction phenomenon, *J. Geophys. Res.*, 103(D6), 1998.
- Isler, J. R., M. J. Taylor, and D. C. Fritts, Observational evidence of wave ducting and evanescence in the mesosphere, *J. Geophys. Res.*, 102(D22), 26301-26313, 1998.
- Kieffaber, L. M., Structure and fluctuations of the OH airglow at 1.65 and 2.15 μm , Ph. D. Thesis, University of New Mexico, Albuquerque, 1973.
- Kitamura, Y., and I. Hirota, Small-scale disturbances in the lower stratosphere revealed by daily rawin sonde observations, *J. Met. Soc. Japan*, 67, 817-831, 1989.
- Lighthill, J., *Waves in Fluids*, Cambridge University Press, New York, 1978.
- Lindzen, R. S., Turbulence and stress due to gravity wave and tidal breakdown, *J. Geophys. Res.*, 86, 9707-9714, 1981.

- Mahapatra, P. R., R. J. Doviak, and D. S. Zrníc, Multisensor observation of an atmospheric undular bore, *Bull. Amer. Met. Soc.*, 72, 1468-1480, 1991.
- Makhlouf, U., E. Dewan, J. R. Isler, and T. F. Tuan, On the importance of purely gravitationally induced density, pressure, and temperature variations in gravity waves: Their application to airglow observations. *J. Geophys. Res.*, 95, 4103-4144, 1990.
- Matsuno, T., A quasi-one dimensional model of the middle atmospheric circulation interacting with internal gravity waves, *J. Met. Soc. Japan.*, 60, 215-266, 1982.
- McLennan, J. C., and G. M. Shrum, On the origin of the auroral green line 5577 Å and other spectra associated with aurora borealis, *Proc. Roy. Soc.*, A108, 501, 1925.
- Meek, C. E., I. M. Reid, and A. H. Manson, Observations of mesospheric wind velocities 2. Cross sections of power spectral density for 48-8 h, 8-1 h, 1 h-10 min over 60-110 km for 1981, *Radio Sci.*, 20, 1383-1402, 1985.
- Meinel, A. B., OH emission bands in the spectrum of the night sky-I. *Astrophys. J.*, 111, 555, 1950a.
- Meinel, A. B., OH emission bands in the spectrum of the night sky-I. *Astrophys. J.*, 112, 120, 1950b.
- Moreels, G. and M. Herse, Photographic evidence of waves around the 85 km level, *Planet. Space Sci.*, 25, 265, 1977.
- Murayama, Y., T. Tsuda, M. Yamamoto, T. Nakamura, T. Sato, S. Kato, and S. Fukao, Dominant vertical scales of gravity waves in the middle atmosphere observed with the MU radar and rocketsondes, *J. Atmos. Terr. Phys.*, 54, 339-346, 1992.
- Nakamura, T., T. Tsuda, M. Yamamoto, S. Fukao, and S. Kato, Characteristics of gravity waves in the mesosphere observed with the middle and upper atmosphere radar, 2, Propagation direction, *J. Geophys. Res.*, 98, 9811, 1996.
- Offermann, D., and A. Drescher, Atomic oxygen densities in the lower thermosphere as derived from in situ 5577 Å night airglow and mass spectrometer measurements, *J. Geophys. Res.*, 78, 6690, 1973.
- Peterson, A. W., Airglow events visible to the naked eye, *App. Opt.*, 18, 3390, 1979.
- Peterson, A. W., and G. W. Adams, OH airglow phenomena during the 5-6 July 1982 total lunar eclipse, *App. Opt.*, 22, 2682, 1983.

- Peterson, A. W., and L. M. Kieffäber, Infrared photography of OH airglow structures. *Nature*, 242, 321, 1973.
- Rees, M. H., *Physics and Chemistry of the Upper Atmosphere*, Cambridge university press, New York, 1989.
- Reid, I. M., Gravity wave motions in the upper middle atmosphere (60-110 km), *J. Atmos. Terr. Phys.*, 48(11-12), 1057, 1986.
- Roach, F. E., and L. L. Smith, The worldwide morphology of the atomic oxygen nightglows, Aurora, and Airglow, in *Proceedings of the NATO Advanced Study Institute, University of Keele, UK*, edited by B. M. McCormac, Reinhold Publishing Corporation, New York, 1967.
- Shibata, T., S. Ichinose, T. Narikiyo, and M. Maeda, Spectral analysis of vertical temperature profiles observed by lidar in the upper stratosphere and the lower mesosphere, *J. Met. Soc. Japan*, 66, 1001-1005, 1988.
- Shibata, T., T. Kukuda, and M. Maeda, Density fluctuations in the middle atmosphere over Fukuoka observed by a XeF Rayleigh lidar, *Geophys. Res. Lett.*, 13, 1121-1124, 1986.
- Swenson, G. R., and S. B. Mende, OH emission and gravity waves (including a breaking wave) in all-sky imagery from Bear Lake, UT., *Geophys. Res. Lett.*, 21, 2239, 1994.
- Swenson, G. R., M. J. Taylor, P. J. Espy, C. Gardner, and X. Tao, ALOHA-93 measurements of intrinsic AGW characteristics using the airborne airglow imager and groundbased Na wind/temperature lidar, *Geophys. Res. Lett.*, 22, 2841, 1995.
- Taylor, M. J., Observation and analysis of wave-like structures in the lower thermospheric nightglow emissions, Ph. D. thesis, Univ. of Southampton, Southampton, UK, 1986a.
- Taylor, M. J., TV observations of mesospheric wave structure, in *Collection of Works of the International Workshop of Noctilucent Clouds*, 153, Valgus, Tallinn, 1986b.
- Taylor, M. J., A review of advances in imaging techniques for measuring short period gravity waves in the mesosphere and lower thermosphere., *Adv. Space Res.*, 19, 667-676, 1997.
- Taylor M. J., M. B. Bishop, and V. Taylor, All-sky measurements of short period waves imaged in the OI (557.7 nm), Na (589.2 nm) and near infrared OH and O₂ (0,1) nightglow emissions during the ALOHA-93 campaign, *Geophys. Res. Lett.*, 22, 2833, 1995a.

- Taylor, M. J., and R. Edwards, Observations of short period mesospheric wave patterns; in situ or tropospheric wave generation?, *Geophys. Res. Lett.*, 18(7), 1337-1340, 1991.
- Taylor M. J., D. C. Fritts, and J. R. Isler, Determination of horizontal and vertical structure of a novel pattern of short period waves during ALOHA-93, *Geophys. Res. Lett.*, 22, 2837, 1995b.
- Taylor M. J., Y. Y. Gu, X. Tao, C. S. Gardner, and M. B. Bishop, An investigation of intrinsic gravity waves signatures using coordinated lidar and nightglow image measurements, *Geophys. Res. Lett.*, 22(20), 2853, 1995c.
- Taylor, M. J., and M. A. Hapgood, Identification of a thunderstorm as a source of short period gravity waves in the upper atmospheric nightglow emissions, *Planet. Space Sci.*, 36(10), 975, 1988.
- Taylor, M. J., and M. A. Hapgood, On the origin of ripple-type wave structure in the OH nightglow emission, *Planet. Space Sci.*, 38(11), 1421, 1990.
- Taylor, M. J., M. A. Hapgood, and P. Rothwell, Observations of gravity wave propagation in the OI (557.7 nm), Na (589.2 nm) and the near infra-red OH nightglow emissions, *Planet. Space Sci.*, 35, 413, 1987.
- Taylor, M. J., and M. J. Hill, Near infrared imaging of hydroxyl wave structure over and ocean site at low latitudes, *Geophys. Res. Lett.*, 18(7), 1333, 1991.
- Taylor, M. J., W. R. Pendleton Jr., and S. Clark, Image measurements of short-period gravity waves at equatorial latitudes, *J. Geophys. Res.*, 102, 26283-26299, 1997.
- Taylor, M. J., E. H. Ryan, T. F. Tuan, and R. Edwards, Evidence of preferential directions for gravity wave propagation due to wind filtering in the middle atmosphere, *J. Geophys. Res.*, 98, 6047, 1993
- Taylor, M. J., G. R. Swenson, and V. Taylor, Height measurements of OI (557.7 nm) gravity wave structure over the Hawaiian Islands during ALOHA-93, *Geophys. Res. Lett.*, 22, 2881, 1995d.
- Taylor, M. J., D. N. Turnbull, and R. P. Lowe, Spectrometric and imaging measurements of a spectacular gravity wave event observed during the ALOHA-93 campaign, *Geophys. Res. Lett.*, 22(20), 2849-2852, 1995e.
- Tricker, R. A. R., *Bores, Breakers, Waves, and Wakes*, Elsevier, New York, 1965.

- Tsuda, T., Y. Murayama, T. Nakamura, R. A. Vincent, A. H. Mason, C. E. Meek, and R. L. Wilson, Variations of the gravity wave characteristics with height, season and latitude revealed by comparative observations, *J. Atmos. Terr. Phys.*, 56(5), 555-568, 1994.
- Tsuda, T., T. E. VanZandt, M. Mizumoto, S. Kato, and S. Fukao, Spectral analysis of temperature and Brunt-Vaisala frequency fluctuations observed by radiosondes, *J. Geophys. Res.*, 96, 17265-17278, 1991.
- Vincent, R. A., Gravity wave motions in the mesosphere, *J. Atmos. Terr. Phys.*, 46, 119-128, 1984.
- Watanabe, T., M. Nakamura, and T. Ogawa, Rocket measurements of O₂ atmospheric and OH Meinel bands in the airglow, *J. Geophys. Res.*, 86, 5768, 1981.
- Wiens, R. H., S. P. Zhang, R. N. Peterson, and G. G. Shepherd, Tides in emission rate and temperature from the O₂ nightglow over Bear Lake Observatory, *Geophys. Res. Lett.*, 22, 2367, 1995.
- Wilson, R. L., M.-L. Chanin, and A. Hauchecorne, Gravity waves in the middle atmosphere as observed by Rayleigh lidar, *J. Geophys. Res.*, 96, 1585-1588, 1990.
- Wilson, R. L., A. Hauchecorne, and M.-L. Chanin, Gravity wave spectra in the middle atmosphere observed by Rayleigh lidar: 2. Climatology, *J. Geophys. Res.*, 96, 5169-5183, 1991.
- Wu, Q., and T. L. Killeen, Seasonal dependence of mesospheric gravity waves (<100 km) at Peach Mountain Observatory, Michigan, *Geophys. Res. Lett.*, 23, 2211, 1996.

APPENDIX

DERIVATION OF THE AGW DISPERSION RELATION

Most parts of the following descriptions are based on the book "The physics of atmospheres" (pp 106 - 108) by *Houghton* [1989].

With reference to section 1.3.2. the components of the momentum equation are:

$$\frac{du}{dt} + \frac{1}{\rho} \frac{\partial p}{\partial x} = 0 \quad (\text{A-1})$$

$$\frac{dw}{dt} + \frac{1}{\rho} \frac{\partial p}{\partial z} = 0 \quad (\text{A-2})$$

where, $u = dx/dt$, $w = dz/dt$, ρ = density of fluid, and p = pressure of fluid

According to the continuity equation:

$$\frac{1}{\rho} \frac{d\rho}{dt} + \frac{\partial u}{\partial x} + \frac{\partial w}{\partial z} = 0 \quad (\text{A-3})$$

According to the first law of thermodynamics, the potential temperature θ

should be constant for adiabatic motion, i.e.:

$$\frac{d \ln \theta}{dt} = 0 \quad (\text{A-4})$$

where θ can be represented in terms of ρ and p such that:

$$\frac{d \ln \theta}{dt} = \frac{1}{\gamma} \frac{d \ln p}{dt} - \frac{d \ln \rho}{dt} \quad (\text{A-5})$$

Neither θ , p nor ρ vary in the horizontal for the unperturbed atmosphere. Now let us introduce small perturbations (represented by a prime) in the velocity components, pressure, and density field due to the wave motion, such that $u = u'$, $w = w'$, $\rho' = \bar{\rho} + \rho'$, and $p' = \bar{p} + p'$, where a component with a bar represent the mean value. Then using the hydrostatic equation:

$$\bar{p}^{-1} (\partial \bar{p} / \partial z) = -H^{-1} \quad (\text{A-6})$$

(where H is the atmospheric scale height), the equation of state:

$$\bar{p} / \bar{\rho} = gH \quad (\text{A-7})$$

ignoring products of primed quantities, the above four equations (A-1), (A-2), (A-3) and (A-5) become for the four unknowns u' , w' , $\rho' / \bar{\rho}$, and p' / \bar{p} :

$$\frac{\partial u'}{\partial x} + gH \frac{\partial}{\partial x} (p' / \bar{p}) = 0 \quad (\text{A-8})$$

$$\frac{\partial w}{\partial z} + g(\rho' / \bar{\rho}) + gH \frac{\partial}{\partial z} (\rho' / \bar{\rho}) - g(\rho' / \bar{\rho}) = 0 \quad (\text{A-9})$$

$$\frac{\partial u}{\partial x} + \frac{\partial w}{\partial z} - \frac{w}{H} + \frac{\partial}{\partial z} (\rho' / \bar{\rho}) = 0 \quad (\text{A-10})$$

$$-Bw' + \frac{\partial}{\partial z} (\rho' / \bar{\rho}) = 0 \quad (\text{A-11})$$

where, the vertical stability parameter B is equal to $\partial \ln \theta / \partial z$. In an isothermal atmosphere, H is constant and thus B is constant and equal to $(\gamma - 1) / \gamma H$.

The following four equations are obtained assuming wave solutions of the form $\exp(\alpha z) \exp i(\omega t + kx + mz)$ (see section 1.3.2.) by substituting into equations (A-8), (A-9), (A-10), and (A-11) for solving for the four unknowns u' , w' , $\rho' / \bar{\rho}$, and p' / \bar{p} , substituting $\alpha = 1 / 2H$ into the equation with $m \neq 0$ (i.e., internal waves). We get:

$$i\omega u' + ikgH(\rho' / \bar{\rho}) = 0 \quad (\text{A-12})$$

$$i\omega w' + g(\rho' / \bar{\rho}) + (-1/2g + imgH)(\rho' / \bar{\rho}) = 0 \quad (\text{A-13})$$

$$ik u' + (-1/2H^2 + im)w' + i\omega(\rho' / \bar{\rho}) = 0 \quad (\text{A-14})$$

$$-B + i\omega(\rho' / \bar{\rho}) - 1/\gamma i\omega(\rho' / \bar{\rho}) = 0 \quad (\text{A-15})$$

The dispersion characteristic AGW relation can then be obtained by making the real part of the determinant of the above coefficients for the four unknowns equal to zero. Let's follow this step by step. Matrix M of the above coefficients of four unknowns is:

$$\begin{array}{cccc}
 i\omega & 0 & 0 & ikgH \\
 M = & 0 & i\omega & g & 1/2 g + imgH & (A-16) \\
 & ik & -\frac{1}{2} H^1 + im & i\omega & 0 \\
 & 0 & -B & i\omega & -i\omega/\gamma
 \end{array}$$

The determinant of M becomes:

$$\begin{aligned}
 \det(M) &= -1/4 (4\omega^4 H - 2\omega^2 g + \omega^2 g\gamma - 4i\omega^2 g\gamma mH + 4i\omega^2 mgH) & (A-17) \\
 &- 4\omega^2 gm^2 H^2 \gamma - 2\omega^2 BgH\gamma + 4i\omega^2 B g H^2 \gamma m \\
 &- 4k^2 g H^2 \gamma \omega^2 + 4k^2 g^2 H^2 \gamma B) / (H\gamma)
 \end{aligned}$$

Setting the real part of the determinant of M to zero gives:

$$\begin{aligned}
 \text{Re}(\det(M)) &= -\omega^4/\gamma + \omega^2 g/(2H\gamma) - \omega^2 g/(4H) + H\omega^2 g m^2 \\
 &+ \omega^2 Bg/2 + Hk^2 g \omega^2 - H k^2 g^2 B \\
 &= 0 & (A-18)
 \end{aligned}$$

Substituting $B = (\gamma - 1)/(\gamma H)$ into (A-18) yields:

$$\begin{aligned}
 \text{Re}(\det(M)) &= -\omega^4/\gamma + \omega^2 g/(2H\gamma) - \omega^2 g/(4H) + H\omega^2 g m^2 \\
 &+ \omega^2 (\gamma - 1)g/(2\gamma H) + Hk^2 g \omega^2 - k^2 g^2 (\gamma - 1)/\gamma \\
 &= 0 & (A-19)
 \end{aligned}$$

If we now solve this equation for m^2 the solution becomes:

$$\begin{aligned} m^2 &= - [-\omega^4 / \gamma + \omega^2 g / (4H) + Hk^2 g \omega^2 - k^2 g^2 + k^2 g^2 / \gamma] / (H\omega^2 g) \\ &= \omega^2 / (\gamma Hg) - (1/4) (1 + 4H^2 k^2) / H^2 + k^2 g (\gamma - 1) / \gamma H\omega^2 \end{aligned} \quad (\text{A-20})$$

By using the following relations,

$$\begin{aligned} \omega_B^2 &\equiv (\gamma - 1)g / (\gamma H) & \text{where, } \omega_B &: \text{Brunt-Vaisala frequency} \\ \omega_a^2 &\equiv \gamma g / (4H) = C^2 / (4H^2) & \omega_a &: \text{acoustic frequency} \end{aligned}$$

m^2 becomes:

$$m^2 = k^2 (\omega_B^2 / \omega^2 - 1) + (\omega^2 - \omega_a^2) / C^2 \quad (\text{A-21})$$

This equation is the dispersion equation of a gravity wave written in the form of the horizontal and vertical wave numbers. The original form as derived by *Hines* [1960] is obtained by multiplying $\omega^2 C^2$ to the above dispersion equation:

$$m^2 \omega^2 C^2 = \omega^4 - \omega^2 C^2 k^2 - \omega^2 \gamma^2 g^2 / (4C^2) + (\gamma - 1) g^2 k^2 \quad (\text{A-22})$$

And substituting $k^2 \equiv k_x^2$ and $m^2 \equiv k_z^2$ into the above equation, we get the following dispersion relation of the other form:

$$\omega^4 - \omega^2 C^2 (k_x^2 + k_z^2) + (\gamma - 1) g^2 k_x^2 - \omega^2 \gamma^2 g^2 / (4C^2) = 0 \quad (\text{A-23})$$

[Hines, 1960]